1-1-2014

Simplified mapping rule for bounding surface simulation of complex loading paths in granular materials

Mojtaba E. Kan
University of New South Wales, mojtaba@uow.edu.au

Hossein Taiebat
University of New South Wales, h.taiebat@unsw.edu.au

Nasser Khalili
University of New South Wales, n.khalil@unsw.edu.au

Simplified mapping rule for bounding surface simulation of complex loading paths in granular materials

Abstract

This paper presents a bounding surface plasticity model that can be used to simulate complex monotonic and cyclic loading paths.A new mapping rule that only uses the last stress reversal point is introduced to describe the stress-strain behavior of granular soils during loading and unloading. This mapping rule is easy to implement and is suitable for highly erratic cyclic loading conditions, e.g., those induced by earth- quake or traffic loading. The application and performance of the model are demonstrated using the results of experimental tests with various stress paths conducted under both monotonic and cyclic loading conditions. The study shows the efficiency of the new mapping rule in cap- turing the characteristic features of the behavior of granular soils under various loading paths.

Publication Details

Kan, M. E., Taiebat, H. A. & Khalili, N. (2014). Simplified mapping rule for bounding surface simulation of complex loading paths in granular materials. International Journal of Geomechanics, 14 (2), 239-253.

A Simplified Mapping Rule for Bounding Surface Simulation of Complex Loading Paths in Granular Materials

Mojtaba E. Kan[1]; Hossein A. Taiebat[2] and Nasser Khalili[3]

Abstract: This paper presents a bounding surface plasticity model that can be used to simulate complex monotonic and cyclic loading paths. A new mapping rule which only uses the last stress reversal point is introduced to describe the stress-strain behaviour of granular soils during loading and unloading. This mapping rule is easy to implement and is suitable for highly erratic cyclic loading condition, e.g. those induced by earthquake or traffic loading. The application and performance of the model is demonstrated using the results of experimental tests with various stress paths conducted under both monotonic and cyclic loading conditions. The study shows the efficiency of the new mapping rule in capturing the characteristic features of the behaviour of granular soils under various loading paths.

Keywords: bounding surface plasticity; mapping rule; cyclic loading; granular soil

[1] Research scholar, School of Civil and Environmental Engineering, The University of New South Wales, Sydney, NSW 2052, Australia. Email: m.esfahanikan@unsw.edu.au

[2] Senior Lecturer, School of Civil and Environmental Engineering, The University of New South Wales, Sydney, NSW 2052, Australia. Email: h.taiebat@unsw.edu.au

[3] Professor, School of Civil and Environmental Engineering, The University of New South Wales, Sydney, NSW 2052, Australia. Email: n.khalil@unsw.edu.au

INTRODUCTION

The concept of bounding surface plasticity was first introduced by Dafalias and Popov (1975) and Krieg (1975) to model nonlinear behaviour of materials under complex loading. In this approach, the plastic deformation at a stress point is calculated by defining the plastic modulus as a decreasing function of the distance of the stress point from its "image point" on a limiting surface called the bounding surface. This provides a smooth transition of stiffness from elastic to elastic-plastic state. By using a three-segmented bounding surface with a simple radial projection rule and a distance dependent additive plastic modulus, Dafalias and Hermann (1980) applied the theory of bounding surface plasticity to cohesive soils. Later, Bardet (1986) extended the application of the bounding surface models to nonlinear irreversible behaviour of sands, including strain softening and stress dilatancy observed in dense sands. This was achieved by defining the plastic modulus as a function of the mean effective stress and the stress ratio. However, the model proposed was based on the associativity of flow rule, and was unable to capture the post-peak strain-softening behaviour of loose sands under undrained shearing. Further developments of the bounding surface model were due to Crouch (1994) for 2D cases and Crouch and Wolf (1994a&b) for 3D cases, in which the combined radial and deviatoric mapping rules, non-associate flow rule, the bi-linear critical state line and the apparent normal consolidation line for sands were included. The shortcomings of this model were the complex shape of bounding surface, lack of continuity between the two mapping regions used in the model and the large number of model parameters.

More recently, a more rigorous bounding surface model based on the concept of the critical state soil mechanics was developed at The University of New South Wales (UNSW) by Russell and Khalili (2004) to model the stress-strain behaviour of sands. Later Khalili *et al.* (2005 & 2008) extended the model to simulate the behaviour of sands subjected to cyclic

loading under saturated and unsaturated states including hydraulic hysteresis effects. In this model, hereafter referred to as UNSW constitutive model, the shape of the bounding surface was obtained from experimental observations of undrained stress path responses of soils at their loosest state. A mapping rule, passing through stress reversal points, was introduced to predict the stress-strain behaviour under loading and unloading. Compared with the classical bounding surface models, UNSW model was able to capture well the characteristic features of granular soils subjected to cyclic loading (e.g. the contraction during deviatoric unloading), as well as the behaviour of normally and over consolidated clayey materials. However, the mapping rule adopted, despite its excellent performance in capturing the cyclic behavior of soils, could not be applied efficiently to highly variable loading paths due to its complex procedure and the storage and memory requirement in a boundary value problem. To tackle this problem, a single stress point mapping rule is introduced in this study which has a simpler procedure and is more amenable to application to complex loading paths. The performance of the new mapping rule is illustrated by comparing the results of simulation of the model using the two mapping rules. The new mapping rule is then employed to simulate the behaviour of different soils under various monotonic and cyclic loading paths.

The novel aspects of the current work are threefold:

- The model formulation is extended to three-dimensional stress space (i.e. $p' - q - \theta$).
- A new mapping rule is introduced which has less complexity and brings more robustness and efficiency in numerical modelling of highly complex cyclic loading paths; e.g. earthquake loading.
- A host of new simulations, for a variety of different stress paths, including conventional drained and undrained triaxial tests, constant mean effective stress tests, constant confining stress tests, anisotropically consolidated and anisotropic compression tests are presented to highlight the capabilities of the model. A single set

of parameters are used for each material in all simulations, though the experimental data are taken from different references in the literature.

PRELIMINARIES

Notation

Soil mechanics sign is adopted throughout. Compression is taken as positive and tension as negative. For the sake of simplicity, all derivations are presented in the $p'-q$ plane in a three-dimensional stress space such that

$$p' = -\frac{I'}{3},\ q = \sqrt{3J_2} \tag{1}$$

where $I' = \boldsymbol{\sigma}^T\boldsymbol{\delta}$ is the first invariant of the effective stress tensor, $J_2 = \frac{1}{2}\left(\mathbf{s}^T\mathbf{s}\right)$ is the second invariant of the deviator stress tensor, $\mathbf{s} = \boldsymbol{\sigma} - \frac{1}{3}\left(\boldsymbol{\sigma}^T\boldsymbol{\delta}\right)\boldsymbol{\delta}$, and δ is Kronecker delta. The corresponding strain conjugates are

$$\varepsilon_v = -\hat{I},\ \varepsilon_q = \frac{2}{\sqrt{3}}\sqrt{\hat{J}_2} \tag{2}$$

where $\hat{I} = \varepsilon^T\boldsymbol{\delta}$ and $\hat{J}_2 = \frac{1}{2}\left(\hat{\mathbf{s}}^T\hat{\mathbf{s}}\right)$ are the first and the second invariants of the strain vector, respectively, and $\hat{\mathbf{s}} = \boldsymbol{\varepsilon} - \frac{1}{3}\left(\boldsymbol{\varepsilon}^T\boldsymbol{\delta}\right)\boldsymbol{\delta}$.

The total strain increments are divided into elastic and plastic components as

$$\dot{\varepsilon} = \dot{\varepsilon}^e + \dot{\varepsilon}^p \tag{3}$$

where the superscripts *e* and *p* denote the elastic and plastic components, respectively. The volumetric strain, ε_v, is related to the specific volume (υ) as

$$\varepsilon_v = \ln(\frac{\upsilon}{\upsilon_0}) \tag{4}$$

where $\upsilon_0 = 1 + e_0$ is the specific volume at the reference mean effective stress, $\upsilon = 1 + e$, and e and e_0 are the current void ratio and the void ratio at the reference point, respectively. The material behaviour is assumed isotropic and rate independent.

Critical State

The critical state is the ultimate condition towards which all states approach with increasing deviatoric shear strain. Figure 1 shows the Critical State Line (CSL) in the $\upsilon - \ln p'$ plane, approximated by two linear segments (after Been *et al.*, 1991). More specifically, four parameters are used to define the critical state line (CSL) in the $\upsilon - \ln p'$ plane: λ_0 and Γ_0 are the slope of the initial portion of the CSL and its specific volume at $p' = 1kPa$, respectively; p'_{cr} is the mean effective stress at the onset of particle crushing; and λ_{cr} is the slope of CSL during the particle crushing stage. A dimensionless state parameter (ξ) is defined as a measure of consistency of the soil under its current state; it is positive on the loose side of CSL and negative on the dense side, and is defined as

$$\xi = \upsilon - \upsilon_{cs} \tag{5}$$

where υ is the specific volume at the current stress, p', and υ_{cs} is the specific volume at the critical state corresponding to p'.

103 The CSL in the $q-p'$ plane is defined as a straight line passing through the origin. Following

104 Sheng *et al.* (2000), the slope of the CSL, M_{cs}, is defined as a function of Lode angle, θ,

105 $$M_{cs}(\theta) = M_{\max}\left(\frac{2\alpha^4}{1+\alpha^4-(1-\alpha^4)\sin 3\theta}\right)^{\frac{1}{4}} \tag{6}$$

106 where θ is defined as $\theta = \frac{1}{3}\sin^{-1}\left(-\frac{3\sqrt{3}}{2}\frac{J_3}{\sqrt{(J_2)^3}}\right)$, J_2 and J_3 are the second and third

107 invariants of stress vector. Lode angle ranges from $\theta = -\frac{\pi}{6}$ for triaxial extension to $\theta = +\frac{\pi}{6}$

108 for triaxial compression. Here, α is a function of the strength parameter of soil and can be

109 given as

110 $$\alpha = \frac{3-\sin\varphi'_{cs}}{3+\sin\varphi'_{cs}} \tag{7}$$

111 where ϕ'_{cs} is the critical state internal frictional angle and is considered independent of

112 crushing of particles. $M_{\max}$ is the value of M_{cs} for triaxial compression which is linked to the

113 critical state friction angle and can be given as

114 $$M_{\max} = \frac{6\sin\phi'_{cs}}{3-\sin\phi'_{cs}} \tag{8}$$

115 The proposed shape of the failure surface coincides with the Mohr-Coulomb failure surface at

116 all vertices in the deviatoric plane. It is also noted that $\alpha = 1$ recovers the von Mises failure

117 surface.

118 The Limiting Isotropic Compression Line (LICL) is defined as parallel to the CSL with a

119 constant shift in $\upsilon - \ln p'$ plane along the recompression line, as shown in Figure 1, Similar to

120 the critical state line, the LICL is a reference line in the $q-p'$ space, which can be viewed as

121 locus of the loosest possible state for a soil under a given mean effective stress. Given the
122 expression of CSL as

123 $$\upsilon = f\left(p'\right) \tag{9}$$

124 the LICL is expressed as

125 $$\upsilon = f\left(\bar{p}'\right) = f\left(p'\right) - \kappa \ln R \tag{10}$$

126 where $\bar{p}' = R.p'$, and R is a model parameter.

127 STRESS STRAIN RELATIONSHIP

128 The incremental elastic strains are linked to the incremental stresses through

129 $$\dot{\boldsymbol{\sigma}}' = \mathbf{D}^e \dot{\boldsymbol{\varepsilon}}^e \tag{11}$$

130 where $\mathbf{D}^e$ is the elastic property matrix which can be defined as a function of the bulk
131 modulus, K, and the shear modulus, G.

132 The incremental plastic strain-stress relationship is written as

133 $$\dot{\boldsymbol{\varepsilon}}^p = \frac{1}{h}\mathbf{m}\mathbf{n}^T \dot{\boldsymbol{\sigma}}' \tag{12}$$

134 where $\mathbf{n}$ is the unit vector normal to the loading surface at the current stress state, $\boldsymbol{\sigma}'$, $\mathbf{m}$ is
135 the unit direction of plastic flow at $\boldsymbol{\sigma}'$, and h is the hardening modulus. Substituting (12) and
136 (3) in (11) the elastic-plastic stress-strain relationship is obtained as

137 $$\dot{\boldsymbol{\sigma}}' = \left(\mathbf{D}^e - \frac{\mathbf{D}^e \mathbf{m}\mathbf{n}^T \mathbf{D}^e}{h + \mathbf{n}^T \mathbf{D}^e \mathbf{m}} \right) \dot{\boldsymbol{\varepsilon}} \tag{13}$$

The bulk and shear elastic moduli are calculated assuming that unloading/reloading occurs along a κ line in the $\upsilon - \ln p'$ plane. The moduli are then defined as

$$K = \frac{\upsilon p'}{\kappa} \tag{14}$$

$$G = \frac{3(1-2\nu)}{2(1+\nu)} \frac{\upsilon p'}{\kappa} \tag{15}$$

where ν is the Poisson's ratio.

ELASTO-PLASTIC BEHAVIOUR

The essential elements of a bounding surface plasticity model are: (i) a bounding surface for describing the limit states of stress; (ii) a loading surface on which the current stress state lies and a mapping rule to find the image point on the bounding surface; (iii) a plastic potential for describing the mode and magnitudes of plastic deformations, and (iv) a hardening rule for controlling the size of the bounding surface and the location of the loading surfaces.

Following the work of Khalili *et al.* (2005), the domain of purely elastic response is assumed to be nil and all deformation is considered elastic-plastic. This is achieved by defining the hardening modulus, *h*, as a decreasing function of the distance between the stress state, $\boldsymbol{\sigma}'$, and an "image point", $\overline{\boldsymbol{\sigma}}'$ on the bounding surface. During loading the size of the loading surface increases so that any unloading/reloading results in elastic-plastic deformation. Detailed definitions of the bounding surface, the loading surface and mapping rule, the plastic potential, and the hardening rule are given in the following sections. The stress conditions on the bounding surface are denoted using a superimposed bar throughout this notes.

Bounding Surface

Accurate descriptions of the bounding surface are required in order to avoid complications in the stress-strain simulations of soil, particularly under undrained conditions. The shape of the bounding surface is best selected experimentally. It can be determined from the undrained response of the material at its loosest state. It should be mentioned that the undrained response of the material in the effective stress space follows the bounding surface when the contribution of elasticity to volume change is negligible. Examining a host of experimental data, Russell and Khalili (2004) and Khalili *et al.* (2005) suggested the following expression for the shape of the bounding surface:

$$F\left(\bar{p}',\bar{q},\bar{\theta},\bar{p}_c'\right)=\left(\frac{\bar{q}}{M_{cs}\left(\bar{\theta}\right)\bar{p}'}\right)^N-\frac{\ln\left(\bar{p}_c'/\bar{p}'\right)}{\ln R}=0 \tag{16}$$

The parameter $\bar{p}_c'$ controls the size of the bounding surface and is a function of the plastic volumetric strain. The material constant R represents the ratio of $\bar{p}_c'$ and the mean effective stress at the intercept of the bounding surface with the CSL in the $q-p'$ space. The constant N controls the curvature of the bounding surface. The effects of different magnitudes of N and R on the three-dimensional shape of the bounding surface are illustrated in Figure 2.

Loading Surface and Mapping Rule

The loading surface is assumed to be of the same shape as the bounding surface. For first time loading these two surfaces are homologous about the origin of the stress coordinate system. In this case, the function for the loading surface takes the form of

$$F\left(p',q,\theta,p_c'\right)=\left(\frac{q}{M_{cs}\left(\theta\right)p'}\right)^N-\frac{\ln\left(p_c'/p'\right)}{\ln R}=0 \tag{17}$$

where p'_c is the isotropic hardening parameter controlling the size of the loading surface as illustrated in Figure 3. The state of stress, $\boldsymbol{\sigma}'$, is always located on the loading surface. An image for the state of stress can be found on the bounding surface, $\bar{\boldsymbol{\sigma}}'$, as shown in Figure 3. The centre of homology, $\boldsymbol{\sigma}'$ and $\bar{\boldsymbol{\sigma}}'$ are used to define the mapping rule. For unloading and reloading conditions, the centre of homology moves to the last point of stress reversal. The point of stress reversal is identified when the product of the normal vector to the bounding surface $(\mathbf{n})$ and the vector of the stress increment $(\dot{\boldsymbol{\sigma}}'_e)$ becomes negative (Pastor *et al*, 1990), where $\dot{\boldsymbol{\sigma}}'_e$ is calculated using the total strain as $\mathbf{D}^e \times \dot{\boldsymbol{\varepsilon}}$. The image of the stress point in the $p'-q$ plane is located using the Pegasus method (Dowell and Jarratt, 1972 and Sloan *et al.*, 2001). Upon stress reversal, a new loading surface is formed with the new centre of homology, as shown in Figure 4a. To maintain similarity with the bounding surface, the loading surfaces undergo kinematic hardening during loading and unloading. This mapping rule is simpler and easier to be implemented as compared to the one used originally by Khalili *et al.* (2005).

In order to locate the image point for unloading/reloading condition, Khalili *et al.* (2005) introduced the maximum loading surface at the point of stress reversal as the local bounding surface and formed a new loading surface at the centre of homology. The image point was then located sequentially by projecting the stress point onto a series of intermediate image points on successive local bounding surfaces each passing through a point of stress reversal (Figure 4b). The loading history of the soil was captured through the stress reversal points and the corresponding maximum loading surfaces. Application of such a complex mapping rule is not efficient in simulation of a boundary value problem with highly erratic cyclic loading paths, such as those that occur under earthquake loading conditions. The history of stress reversal points and the geometry of intermediate local bounding surfaces should also be

tracked during unloading/reloading conditions, which increases the memory requirement in a large boundary value problem.

The new single stress point mapping rule, proposed in this study, locates the image point directly on the bounding surface, as shown in Figure 4a, without forming successive intermediate local bounding surfaces. This version of the mapping rule is easier to be implemented, does not require the history of previous loading surfaces, and is more suitable for simulation of high frequency cyclic loading, e.g. due to earthquake, vibration, traffic loading and blasting and real life applications where previous stress history of the soil is unknown.

The unit normal vector at the image point defining the direction of loading is given using the general equation:

$$\mathbf{n} = \frac{\partial F / \partial \bar{\boldsymbol{\sigma}}'}{\left\| \partial F / \partial \bar{\boldsymbol{\sigma}}' \right\|} \tag{18}$$

The vector $\partial F / \partial \bar{\boldsymbol{\sigma}}'$ is evaluated applying the chain rule of differentiation:

$$\frac{\partial F}{\partial \bar{\sigma}'} = \frac{\partial F}{\partial \bar{p}'} \frac{\partial \bar{p}'}{\partial \bar{\sigma}'} + \frac{\partial F}{\partial \bar{q}'} \frac{\partial \bar{q}'}{\partial \bar{\sigma}'} + \frac{\partial F}{\partial \bar{\theta}'} \frac{\partial \bar{\theta}'}{\partial \bar{\sigma}'} \tag{19}$$

Recalling the generalized definitions of the invariants $\bar{p}', \bar{q}$ and $\bar{\theta}$, their derivatives with respect to $\bar{\boldsymbol{\sigma}}'$ become

$$\frac{\partial \bar{p}'}{\partial \bar{\boldsymbol{\sigma}}'} = -\frac{1}{3}\boldsymbol{\delta} \tag{20}$$

$$\frac{\partial \bar{q}'}{\partial \bar{\boldsymbol{\sigma}}'} = \frac{3}{2\bar{q}} \left(\bar{\boldsymbol{\sigma}}' - \boldsymbol{\delta} \frac{\bar{I}}{3} \right) \tag{21}$$

$$\frac{\partial \bar{\theta}}{\partial \bar{\boldsymbol{\sigma}}'} = -\frac{\sqrt{3}}{2\sqrt{\bar{J}_2^3}\cos 3\bar{\theta}}\left(\frac{\partial \bar{J}_3}{\partial \bar{\boldsymbol{\sigma}}'} - \frac{3\bar{J}_3}{2\bar{J}_2}\frac{\partial \bar{J}_2}{\partial \bar{\boldsymbol{\sigma}}'}\right) \tag{22}$$

$\partial F/\partial \bar{p}'$, $\partial F/\partial \bar{q}$ and $\partial F/\partial \bar{\theta}$ are evaluated by differentiating the generalized form of equation (16) with respect to $\bar{p}'$, $\bar{q}$ and $\bar{\theta}$

$$\frac{\partial F}{\partial \bar{p}'} = -\frac{N}{\bar{p}'}\left(\frac{\bar{q}}{M_{cs}\left(\bar{\theta}\right)\bar{p}'}\right)^N + \frac{1}{\bar{p}'\ln R} \tag{23}$$

$$\frac{\partial F}{\partial \bar{q}} = \frac{N}{M_{cs}\left(\bar{\theta}\right)\bar{p}'}\left(\frac{\bar{q}}{M_{cs}\left(\bar{\theta}\right)\bar{p}'}\right)^{N-1} = \frac{N}{\bar{q}}\left(\frac{\bar{q}}{M_{cs}(\bar{\theta})\bar{p}'}\right)^N \tag{24}$$

$$\frac{\partial F}{\partial \bar{\theta}} = -\frac{3N}{4}\left(\frac{\bar{q}}{M_{cs}\left(\bar{\theta}\right)\bar{p}'}\right)^N\left(\frac{\left(1-\alpha^4\right)\cos 3\bar{\theta}}{1+\alpha^4-\left(1-\alpha^4\right)\sin 3\bar{\theta}}\right) \tag{25}$$

Plastic Potential

The plastic potential defines the direction of plastic strain increments. Since plastic behaviour is characterized by the link between strain increments and stresses, the plastic potential is generally expressed using a plastic flow rule relating the plastic dilatancy ($d = \dot{\varepsilon}_v^p/\dot{\varepsilon}_q^p$) to the stress ratio q/p'. In this work, the plastic potential (g) is defined as

$$g\left(p', q, \bar{\theta}, p_o\right) = \tilde{t}q + \frac{AM_{cs}\left(\bar{\theta}\right)p'}{A-1}\left(\left(\frac{p'}{p_o}\right)^{A-1} - 1\right) \quad \text{for } A \neq 1 \tag{26}$$

$$g\left(p', q, \bar{\theta}, p_o\right) = \tilde{t}q + M_{cs}\left(\bar{\theta}\right)p'\ln\left(\frac{p'}{p_o}\right) \quad \text{for } A = 1 \tag{27}$$

where p_0 controls the size of the plastic potential, though it is not required in the model since only derivatives of the (g) function are incorporated in formulations, and A is a material parameter. The direction of plastic flow is defined by:

$$\mathbf{m} = \frac{\partial g / \partial \boldsymbol{\sigma}'}{\left\| \partial g / \partial \boldsymbol{\sigma}' \right\|} \tag{28}$$

in which $\partial g / \partial \boldsymbol{\sigma}'$ is evaluated applying the chain rule of differentiation:

$$\frac{\partial g}{\partial \boldsymbol{\sigma}'} = \frac{\partial g}{\partial p'} \frac{\partial p'}{\partial \boldsymbol{\sigma}'} + \frac{\partial g}{\partial q} \frac{\partial q}{\partial \boldsymbol{\sigma}'} + \frac{\partial g}{\partial \bar{\theta}} \frac{\partial \bar{\theta}}{\partial \boldsymbol{\sigma}'} \tag{29}$$

$\partial g / \partial p'$, $\partial g / \partial q$ and $\partial g / \partial \theta$ are evaluated by differentiating the plastic potential with respect to p', q and $\bar{\theta}$.

$$\frac{\partial g}{\partial p'} = A \left(M_{cs}\left(\bar{\theta}\right) - \tilde{t} \frac{q}{p'} \right) \tag{30}$$

$$\frac{\partial g}{\partial q} = \tilde{t} \tag{31}$$

$$\frac{\partial g}{\partial \bar{\theta}} = -\tilde{t} \frac{3q}{4} \left(\frac{(1-\alpha^4)\cos 3\bar{\theta}}{1+\alpha^4-(1-\alpha^4)\sin 3\bar{\theta}} \right) \tag{32}$$

In the above equations $\tilde{t}$ is a scalar, the sign of which controls the direction of plastic flow in the deviatoric plane. At any stress point two vectors of plastic flow are identified, one corresponding to compressive loading (m^+) and the other to extensive (m^-) as shown in Figure 5. The direction of plastic flow is controlled by $\tilde{t}$, which is determined based on the relative positions of the stress point, $\boldsymbol{\sigma}'$, and its image point, $\bar{\boldsymbol{\sigma}}'$, by comparing the angle

between a given reference axis and the stress point (γ_σ) and the angle between the reference axis and the image point ($\gamma_{\bar{\sigma}}$):

$$\tilde{t} = +1 \qquad \text{for } \left|\gamma_{\bar{\sigma}} - \gamma_\sigma\right| < \pi/2 \tag{33}$$

$$\tilde{t} = -1 \qquad \text{for } \left|\gamma_{\bar{\sigma}} - \gamma_\sigma\right| > \pi/2 \tag{34}$$

Hardening Modulus

In the bounding surface plasticity, the hardening modulus *h* consist of two components

$$h = h_b + h_f \tag{35}$$

where h_b is the plastic modulus at $\bar{\boldsymbol{\sigma}}'$ on the bounding surface, and h_f is plastic modulus at $\boldsymbol{\sigma}'$ and defined as a function of the distance between $\boldsymbol{\sigma}'$ and $\bar{\boldsymbol{\sigma}}'$. Applying the consistency condition at the bounding surface and assuming isotropic hardening of the bounding surface with plastic volumetric compression, the derivative of the bounding surface can be obtained as

$$\dot{F} = \left(\frac{\partial F}{\partial \boldsymbol{\sigma}'}\right)^T \dot{\boldsymbol{\sigma}}' + \frac{\partial F}{\partial \bar{p}_c'} \frac{\partial \bar{p}_c'}{\partial \varepsilon_v^p} \dot{\varepsilon}_v^p \tag{36}$$

Then, the flow rule will be

$$\dot{\varepsilon}_v^p = \dot{\Lambda} \frac{\partial g}{\partial p'} \tag{37}$$

Using the definition of the unit vector normal to the bounding surface, equation (37) can be rewritten as

$$\dot{F} = \mathbf{n}^T \dot{\boldsymbol{\sigma}}' - \dot{\Lambda} h_b = 0 \tag{38}$$

266 in which h_b is calculated as

267 $$h_b = -\frac{\partial F}{\partial \overline{p}'_c}\frac{\partial \overline{p}'_c}{\partial \varepsilon_v^p}\frac{m_p}{\left\|\partial F/\partial \overline{\boldsymbol{\sigma}}'\right\|} \tag{39}$$

268 with $m_p = \dfrac{\partial g/\partial \overline{p}'}{\left\|\partial g/\partial \boldsymbol{\sigma}'\right\|}$. Differentiating equation (16) with respect to $\overline{p}'_c$ yields to

269 $$\frac{\partial F}{\partial \overline{p}'_c} = \frac{-1}{\overline{p}'_c \ln R} \tag{40}$$

270 For isotropic hardening rule, the evolution of $\overline{p}'_c$ with ε_v^p is in turn given by

271 $$\frac{\partial \overline{p}'_c}{\partial \varepsilon_v^p} = \frac{\upsilon \overline{p}'_c}{\lambda - \kappa} \tag{41}$$

272 where λ is the current slope of the LICL in the $\upsilon - \ln p'$. Substituting equations (40) and (41)

273 into equation (39) yields

274 $$h_b = \frac{\upsilon}{(\lambda - \kappa)\ln R}\frac{m_p}{\left\|\partial F/\partial \overline{\boldsymbol{\sigma}}'\right\|} \tag{42}$$

275 The modulus h_f is defined such that it is zero on the bounding surface and infinity at the point

276 of stress reversal, and can take from of

277 $$h_f = \frac{\upsilon p'}{(\lambda - \kappa)}\left(\frac{\overline{p}'_c}{p'_c} - 1\right)k_m\left(\eta_p - \tilde{t}\eta\right) \tag{43}$$

278 where $\overline{p}_c{}'$ and p'_c define the sizes of the bounding and loading surfaces, respectively, η_p is

279 the slope of the peak strength line in the $q - p'$ plane, and k_m is a scaling parameter

280 controlling the steepness of the response in the $q - \varepsilon_q$ plane. The slope of the peak strength

line is a function of the state parameter and the slope of the critical state line, which is given as

$$\eta_p = \tilde{t}\left(1-k\xi\right)M_{cs} \tag{44}$$

where k is a material parameter.

The scaling parameter k_m can be taken as a material constant for some soils, though it is strongly influenced by the initial state parameters and the loading direction (Khalili *et al.*, 2005). Russell and Khalili (2004&2006), examined a wide range of triaxial tests on granular materials and concluded that k_m can be expressed as a function of the initial value of the dimensionless state parameter, ξ_0 (equation 5) and initial confining pressure, p'_0. In this study a general expression for k_m is suggested as follows:

$$k_m = k_{m0}\langle 1.0 - \beta_1 \exp(\xi_0)\rangle (p'_0)^{\beta_2} \tag{45}$$

where k_{m0}, β_1 and β_2 are material parameters.

APPLICATION

To demonstrate robustness and application of the model, a series of comparative simulations is first performed using the new and the original mapping rules (Khalili *et al.*, 2005). This is followed by a host of non-standard monotonic and complex cyclic simulations.

Performance of the New Mapping Rule

To examine the effect of the mapping rule on the performance of the model, cyclic responses of Hostun, Fuji River and Toyoura sands are investigated.

The results of the drained cyclic test simulation on a dense sample of Hostun sand using the original mapping rule (Khalili *at al*. (2005) and the simplified one are presented in Figure 6. Also shown in this figure are the experimental data reported by Saada *et al.* (1989). The initial conditions of the sample were $p' = 350kPa$ and $\upsilon = 1.61$ and the material parameters are selected as $\kappa = 0.003$, $\nu = 0.1$, $M_{cs} = 1.31$, $\lambda_0 = 0.028$, $\lambda_{cr} = 0.24$, $\Gamma_0 = 2.037$, $N = 2.3$, $R = 7.5$, $A = 1.0$ and $k = 2.0$ with $k_m = 3.5$ for the first time loading and $k_m = 35.0$ for unloading and reloading, similar to those used by Khalili *et al.* (2005).

Figure 6 shows that the performance of the new mapping rule is as good as that of the more complex original mapping rule when compared with the results of the experimental data. Both mapping rules capture the stiffening of the material response during unloading and reloading, simulate the contraction of the sample during unloading and the subsequent dilation during reloading. A better match with the experimental data could have been achieved if the model properties were calibrated for the new mapping rule however this was avoided for the sake of consistency of the comparisons.

Figure 7 shows the results of simulation of a cyclic drained test on loose Fuji River sand conducted by Tatsuoka and Ishihara (1974), where the variations of stress ratio versus deviatoric and volumetric strains are presented. In this test the amplitude of the cyclic loading increases gradually at each cycle. The initial conditions of the sample were $p' = 196kPa$ and $\upsilon = 1.74$. The basic material parameters are selected according to those used by Khalili *et al.* (2005), i.e., $\kappa = 0.01$, $\nu = 0.3$, $M_{cs} = 1.48$, $\lambda_0 = 0.032$, $\lambda_{cr} = 0.21$, $\Gamma_0 = 1.870$, $N = 3.0$, $R = 6.2$, $A = 1.0$ and $k = 2.0$; with $k_m = 0.13$ for the first time loading and $k_m = 8.0$ for unloading and reloading.

The results of the simulations show that both mapping rules capture the main features of the behavior of the sand under cyclic loading. The predictions of the two mapping rules are very

similar, except that the new mapping rule predicts a larger volumetric strain than the original mapping rule. However, when compared with the experimental data, the performance of the new mapping rule can be regarded to be as good as the original mapping rule. Figure 7 shows that simplifications of the original mapping rule do not affect the performance of the model, in particular, in simulation of the contractive responses during loading and unloading and the stiffening of the behaviour with successive cycles.

The effects of the two mapping rules on the response of the model are also shown in Figure 8, where the results of simulation for a drained cyclic test on Toyoura sand with constant mean effective stress (Pradhan *et al.* 1989b) are presented. The material parameters and state variables are taken to be the same in both simulations, i.e., $p' = 98.1kPa$, $\upsilon = 1.845$ $\kappa = 0.001$, $\nu = 0.3$, $M_{cs} = 1.24$, $\lambda_0 = 0.03$, $\lambda_{cr} = 0.24$, $\Gamma_0 = 1.969$, $N = 3.0$, $R = 5.8$, $A = 1.0$, $k = 2.0$; with $k_m = 1.0$ for the first time loading and $k_m = 3.0$ for unloading and reloading. Once again both simulations result in very close match with the experimental data. Figure 8 shows noticeable differences in the volumetric strains predicted by the two mapping rules, especially under low cyclic load amplitudes; the volumetric strain is overestimated by the original mapping rule and underestimated by the new mapping rule, when compared with the experimental data. However, under higher cyclic amplitude the performance of the model with the new mapping rule is superior to that with the original mapping rule.

A comparison of the results of the simulations of the model using the two mapping rules indicates that the simplification of the original mapping rule does not affect the performance of the model, especially when the results are compared with the experimental data. The new mapping rule has the advantages of being robust and simpler than the original one and therefore is recommended to be used for complex cyclic loading.

Further Validation

To further examine the performance of the model with the new mapping rule a number of well documented cases from literature are selected and analyzed, such as tests on Nevada sand (Arulmoli et al., 1992) and Toyoura sand (Verdugo and Ishihara, 1996, and Pradhan *et al.*, 1989a). The material parameters used for these simulations are listed in Table 1 and Table 2. The procedure to obtain the material parameters are described by Russell and Khalili (2004) and Khalili *et al.* (2005).

Drained and Undrained Tests on Nevada Sand

Nevada sand was used in VELACS project (Arulmoli *et al.*, 1992) under both 1g laboratory conditions and in centrifuge experiments. The triaxial experiments reported in that project are used here for calibration purpose as well as for verification of the performance of the model. Kutter *et al.* (1994) and Chen (1995) have also reported the results of a series of triaxial and torsional shear tests on Nevada sand which are used in this study for definition of the material properties. Samples of the triaxial tests in VELACS project were 63.5*mm* in diameter and prepared using dry pluviation method. The samples were subjected to a variety of non-standard drained and undrained monotonic stress paths, among them are those of triaxial compression tests shown in Figure 9. The triaxial experiments were performed on both loose $(D_r = 40\%)$ and dense $(D_r = 60\%)$ samples under different confining pressures. The material parameters are shown in Table 1and Table 2.

The results of the simulation of CIDC tests (Figure 9) on loose as well as dense samples of Nevada sand are presented in Figure 10 and Figure 11, respectively. These tests were conducted under drained conditions where the samples were loaded isotropically under 3 different confining pressures of $p_0' = 40, 80, 160 kPa$, followed by loading under constant mean effective stresses. The model captures the experimentally observed initial hardening

behaviour of loose sands accompanied by a volumetric contraction until the critical state is reached (Figure 10). For the dense sand the experimental data do not show a clear softening due the fact that the tests were conducted under constant mean effective stress and the model captures such a behaviour (Figure 11). Overall the prediction of the model is in strong agreement with the test data.

The results of the simulation of CIUC tests (Figure 9) are presented in Figure 12 and Figure 13, for loose and dense samples, respectively. These tests were conducted in undrained conditions under 3 different confining pressures. The model predicts stiffer response initially, but the overall response matches the experimental data very well, especially in $q - p'$ plane.

Figure 14 and Figure 15 show the results of simulation of CADC tests under drained conditions, during which samples of sand were first loaded isotropically to p_0', followed by a loading under constant mean effective stress, followed by a standard triaxial loading to a mean effective stress of p_1'. The samples were then loaded to failure under constant mean effective stress and under constant deviatoric stress, as shown in Figure 9 by $OO_1A_1A_2C_2$ and $OO_1A_1A_2C_4$ stress paths, respectively. The tests were performed at relative densities of $D_r = 40\%$ and 60%. In both cases the model simulates the experimental behaviour very well. The main features of the response, including the peak strength in $q - \varepsilon_1$ plane as well as the initial contraction followed by the progressive dilation in $\varepsilon_v - \varepsilon_1$ plane were captured by the model. It is worth to mention that in CADC tests stress reversal occurs at point A_2 (refer to Figure 9).

Drained and Undrained Tests on Toyoura Sand

Toyoura sand has been used extensively by scholars for verification of different constitutive models (e.g. Khalili *et al.*, 2005, Ling and Yang, 2006). In this study the experimental data on

Toyoura sand reported by Verdugo and Ishihara (1996) are used to verify the performance of the UNSW model. The material parameters obtained by calibration of the model with these tests are also used later to evaluate the performance of the model in simulating a different series of tests reported by Pradhan *et al.* (1989a). The material parameters used for simulation of these tests are shown in Table 1and Table 2.

Verdugo and Ishihara (1996) performed a series of drained and undrained monotonic triaxial tests on Toyoura sand. The specimens were prepared using moist placement method. In the drained tests, two different confining pressures of 100 and $500kPa$ were used for specimens with three different void ratios, ranging from 0.81 to 0.996. The undrained tests were conducted under a wider range of confining pressures, from 100 to 3000 kPa with different void ratios corresponding to relative densities of $D_r = 16\%$ to 64%, corresponding to consistencies from very loose to dense states for the soil under practical stress levels.

The results of the simulations of drained tests under $p_0' = 100kPa$ and $500kPa$ are shown in Figure 16 and compared with experimental data. While there is a slight discrepancy between the predicted performance and experimental data for the loose sample under the low confining pressure, i.e. in test 3, the model predictions for other samples are in excellent agreement with the observed data.

The performance and capability of the model to simulate the undrained behaviour of sands on a wide range of initial conditions, including different relative densities and mean effective stresses, are investigated using 7 undrained tests reported by Verdugo and Ishihara (1996). The outcomes of these simulations are compared with the experimental data in Figure 17 for mean effective stresses vary from 100 to 3000 kPa . In general, the comparison shows satisfactory results, considering the fact that a single set of parameters is used for all simulations under a large range of confining pressures.

The parameters calibrated from the experiments of Verdugo and Ishihara (1996) are also used to simulate the drained behaviour of Toyoura sand reported by Pradhan *et al.* (1989a). The experiments were conducted under various stress paths, including tests to failure under constant axial stress, constant mean effective stress and constant radial pressure, as well as conventional triaxial test (CTC) as shown in Figure 18

Figure 19 compares the results of simulations with the experimental data. The model captures all features of the soil behaviour for different stress paths, with some minor discrepancies where maximum large stress ratio is approached. This may be due to the fact that the Toyoura sand used by Pradhan *et al.* (1989a) was of a different batch from Verdugo and Ishihara (1996), and therefore requires slightly different parameters.

Cyclic Drained tests on Toyoura sand

Pradhan *et al.* (1989b) performed a series of drained triaxial cyclic tests on Toyoura sand. Four cyclic drained tests with constant mean effective stress are selected and used in this study. To highlight the robustness of the proposed model, the material parameters obtained from model calibration with the experimental tests conducted by Verdugo and Ishihara (1996) are used in these simulations. The state parameters and initial conditions of the samples are presented inTable 3.

Figure 20 and Figure 21 show results of drained cyclic tests conducted under constant mean effective stresses on loose and dense samples of Toyoura sand. In these tests the amplitude of the shear strain increases during cyclic loading. These figures show that the model can simulate well the stress-strain response and the successive stiffening or softening of the samples with cyclic loading. The results of the simulation under higher stress levels match better with the experimental data. This may be due the fact that the model parameters are

obtained based on tests conducted on a range of stress levels, mostly greater than $1000kPa$, which are greater than those used in Pradhan *et al.* (1989b) experimental tests, which are all under $100kPa$.

Figure 22 shows the results of simulation of a drained cyclic test with a constant mean effective stress on a very loose sample of Toyoura sand. In this test the amplitude of the shear strain decreases during cyclic loading. This figure also shows the results of a simulation performed by Ling and Yang (2006). The UNSW model captures the general behaviour observed in the experiment, especially in the $\eta - \varepsilon_q$ plane. In $\varepsilon_v - \varepsilon_q$ plane the simulation shows a lower volume change in the median cycles compared to the experimental data. Figure 22 shows the superior performance of the model over that presented by Ling and Yang (2006).

Figure 23 represents the results of simulation of a drained cyclic test on a very loose sample of Toyoura sand under a constant mean effective stress and small hysteresis loops of unloading and reloading. Once again, the model predicts the main features of the behaviour, both in $\eta - \varepsilon_q$ plane and $\varepsilon_v - \varepsilon_q$ plane. It is worth mentioning that a better match between the results of simulation and the test data could have been achieved if the model parameters were calibrated for the same test rather than taking from those calibrated for tests performed by Verdugo and Ishihara (1996).

Cyclic Undrained tests on Fuji River sand

Ishihara *et al.* (1975) conducted a series of undrained triaxial cyclic tests on loose samples of Fuji River sand to study the liquefaction phenomena. Loose samples were obtained by spooning freshly boiled sand into the mold filled with de-aired water. Two of these tests are selected for simulation to show the performance of UNSW model in capturing the undrained behaviour of granular materials. The material parameters and the initial conditions of the samples are listed in Table 1 and

Table 3, respectively. A constant value of k_m is used in these simulations due to the narrow range of initial state parameters, as shown in Table 2.

Figure 24 presents the results of the undrained test conducted on loose Fuji River sand under a cyclic loading with constant stress amplitude. Figure 25 shows the results for a test under irregular cyclic stress amplitude. In both simulations the predicted behaviour is in good agreement with the observed experimental data. The model captures the failure of the samples by liquefaction in which the effective normal stress decreases progressively until the stress path reaches the critical state and the material becomes unstable.

CONCLUSION

The UNSW bounding surface plasticity model has been proved to be a versatile constitutive model capable of simulating the behaviour of sands over a wide range of stresses under drained/undrained and monotonic/cyclic loading conditions. A relatively complex mapping rule was initially formulated for the model which makes application of the model to simulation of highly variable cyclic loading inefficient. In this study, a new mapping rule is formulated which is less complex and more efficient for simulation of complex monotonic and cyclic loadings of granular soils. The new mapping rule does not require a record of history of successive intermediate local bounding surfaces, as was required in the original mapping rule. Comparison of the results of simulations of the model using the original and the new mapping rules indicated that the simplification incorporated in the new mapping rule does not compromise the performance of the model. The robustness of the UNSW model with the new mapping rule was demonstrated through simulations of static and cyclic loading under drained and undrained conditions for different soils. The results of simulations were invariably in excellent agreement with experimental data. The model captures the characteristic features of the behaviour of different sands for a wide range of densities and

stresses, including the stress softening and dilatancy during drained loading of dense sands, liquefaction of loose sands under undrained loading conditions, and the progressive stiffening as well as hysteresis in the stress-strain relationships for cyclic loading. The versatility of the model in simulation of particular sand was demonstrated using one set of material parameters for all tests conducted on the sand under different conditions and by different investigators.

Acknowledgements

The first author is the recipient of the Endeavour Postgraduate Award, Funded by the Australian Government via Department of Education, Employment and Workplace Relations (DEEWR). The support of DEEWR is gratefully acknowledged.

References

Arulmoli, K., Muraleetharan, K., Hossain, M., & Fruth, L. (1992). VELACS: Verification of liquefaction analyses by centrifuge studies, laboratory testing program, soil data report. *Research Report, The earth Technology Corporation*.

Bardet, J. (1986). Bounding surface plasticity model for sands. *Journal of Engineering Mechanics*, *112*(11), 1198-1217.

Been, K., Jefferies, M., & Hachey, J. (1991). The critical state of sands. *Geotechnique*, *41*(3), 365-381.

Chen, Y. R. (1995). *Behavior of a fine sand in triaxial, torsional and rotational shear tests.* PhD thesis, University of California, Davis.

Crouch, R. S. (1994). Unified Critical State Bounding Surface Plasticity Model for Soil. *Journal of Engineering Mechanics*, *120*(11), 2251-2270.

Crouch, R. S., & Wolf, J. P. (1994a). Unified 3D critical state bounding surface plasticity model for soils incorporating continuous plastic loading under cyclic paths. Part II: Calibration and simulations. *International Journal for Numerical and Analytical Methods in Geomechanics, 18*(11), 759-784.

Crouch, R., & Wolf, J. (1994b). Unified 3D critical state bounding-surface plasticity model for soils incorporating continuous plastic loading under cyclic paths. Part I: constitutive relations. *International Journal for Numerical and Analytical Methods in Geomechanics, 18*(11), 735-758.

Dafalias, Y., & Popov, E. (1975). A model of nonlinearly hardening materials for complex loading. *Acta Mechanica, 21*(3), 173-192.

Dafalias, Y. F., & Herrmann, L. R. (1980). A bounding surface soil plasticity model. *International Symposium on Soils under Cyclic and Transient Loading*, Swansea.

Dowell, M., & Jarratt, P. (1972). The "Pegasus" method for computing the root of an equation. *BIT Numerical Mathematics, 12*(4), 503-508.

Ishihara, K., Tatsuoka, F., & Yasuda, S. (1975). Undrained deformation and liquefaction of sand under cyclic stresses. *Soils and Foundations, 15*(1), 29-44.

Khalili, N., Habte, M., & Valliappan, S. (2005). A bounding surface plasticity model for cyclic loading of granular soils. *International journal for numerical methods in engineering, 63*(14), 1939-1960.

Khalili, N., Habte, M., & Zargarbashi, S. (2008). A fully coupled flow deformation model for cyclic analysis of unsaturated soils including hydraulic and mechanical hystereses. *Computers and Geotechnics, 35*(6), 872-889.

Krieg, R. (1975). A practical two surface plasticity theory. *Journal of applied mechanics, ASME, 42*, 641.

Kutter, B. L., Chen, Y. R., & Shen, C. (1994). Triaxial and torsional shear test results for sand, *Contract Report CR 94.003-SHR, Naval Facilities Engineering Service Center*. Port Hueneme, CA 93043-4328.

Ling, H. I., & Yang, S. (2006). Unified sand model based on the critical state and generalized plasticity. *Journal of Engineering Mechanics, 132*(12), 1380-1391.

Pastor, M., Zienkiewicz, O., & Chan, A. (1990). Generalized plasticity and the modelling of soil behaviour. *International Journal for Numerical and Analytical Methods in Geomechanics, 14*(3), 151-190.

Pradhan, T., Tatsuoka, F., Mohri, Y., & Sato, Y. (1989a). An atomated triaxial testing system using a simple triaxial cell for soils. *Soils and Foundations, 29*(1), 151-160.

Pradhan, T., Tatsuoka, F., & Sato, Y. (1989b). Experimental stress-dilatancy relations of sand subjected to cyclic loading. *Soils and Foundations, 29*(1), 45-64.

Russell, A. R., & Khalili, N. (2004). A bounding surface plasticity model for sands exhibiting particle crushing. *Canadian Geotechnical Journal, 41*(6), 1179-1192.

Russell, A., & Khalili, N. (2006). A unified bounding surface plasticity model for unsaturated soils. *International Journal for Numerical and Analytical Methods in Geomechanics, 30*(3), 181-212.

Saada, A., Puccini, P., & Bianchini, G. (1989). Information package. In A. Saada & G. Bianchini (Eds.), *Constitutive Equations for Granular Non-Cohesive Soils*, pp. 81-87. Rotterdam: Balkema.

Sheng, D., Sloan, S., & Yu, H. (2000). Aspects of finite element implementation of critical state models. *Computational mechanics, 26*(2), 185-196.

Sloan, S. W., Abbo, A. J., & Sheng, D. (2001). Refined explicit integration of elastoplastic models with automatic error control. *Engineering Computations, 18*(1/2), 121-194.

Tatsuoka, F., & Ishihara, K. (1974). Drained deformation of sand under cyclic stresses reversing direction. *Soils and Foundations, 14*(3), 51-65.

Verdugo, R., & Ishihara, K. (1996). The steady state of sandy soils. *Soils and Foundations, 36*(2), 81-91.

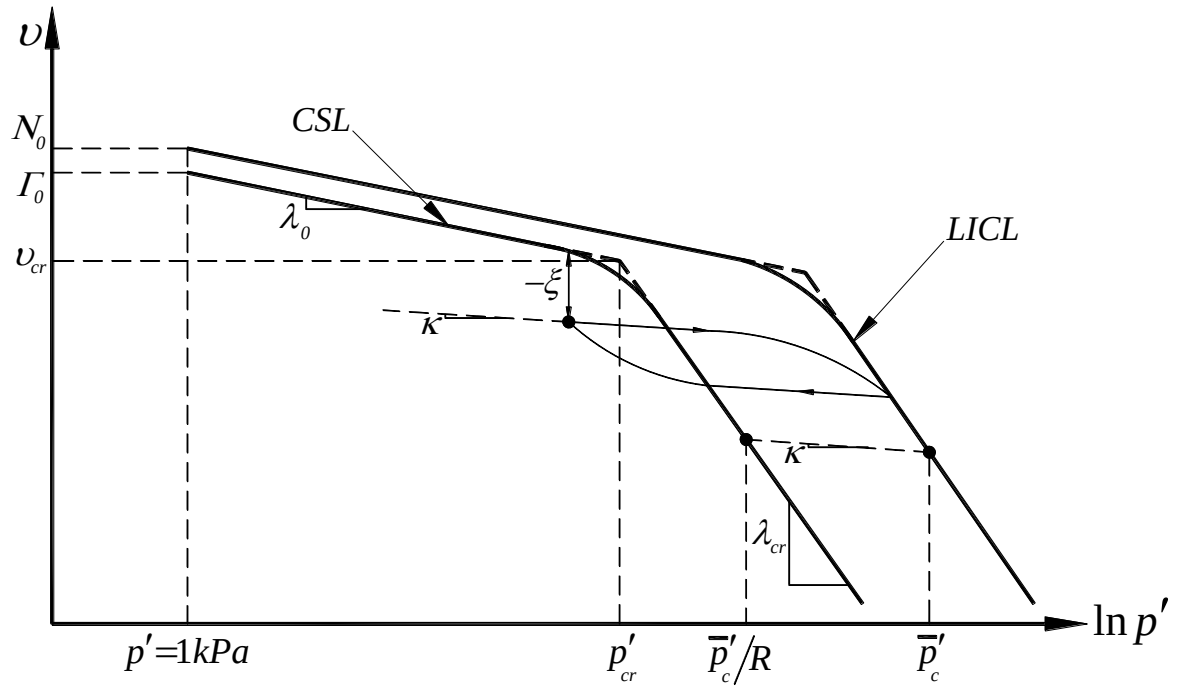

564

565 **Figure 1: Critical State Line (CSL) and Limiting Isotropic Compression Line (LICL)**

566

567

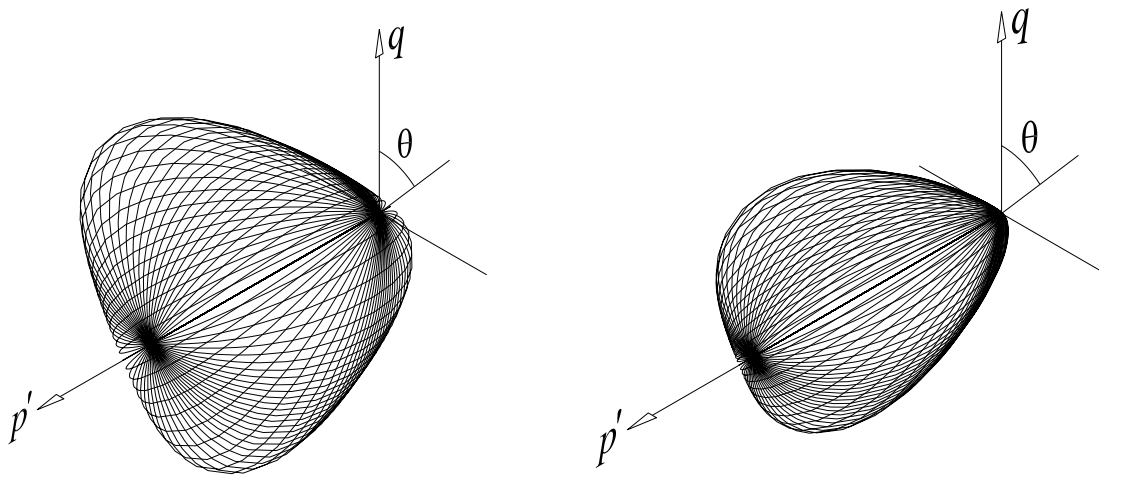

$N=2.0, R=2.0$ $N=2.0, R=6.0$

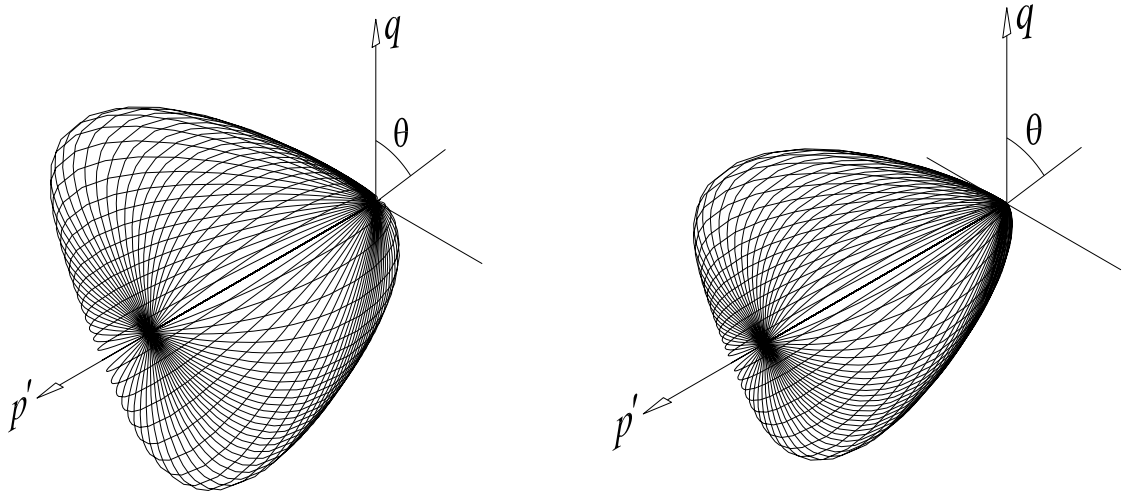

$N=3.0, R=2.0$ $N=3.0, R=6.0$

568 **Figure 2: Effect of N and R on the shape of the bounding surface in $p'-q-\theta$**

569 **space**

570

571

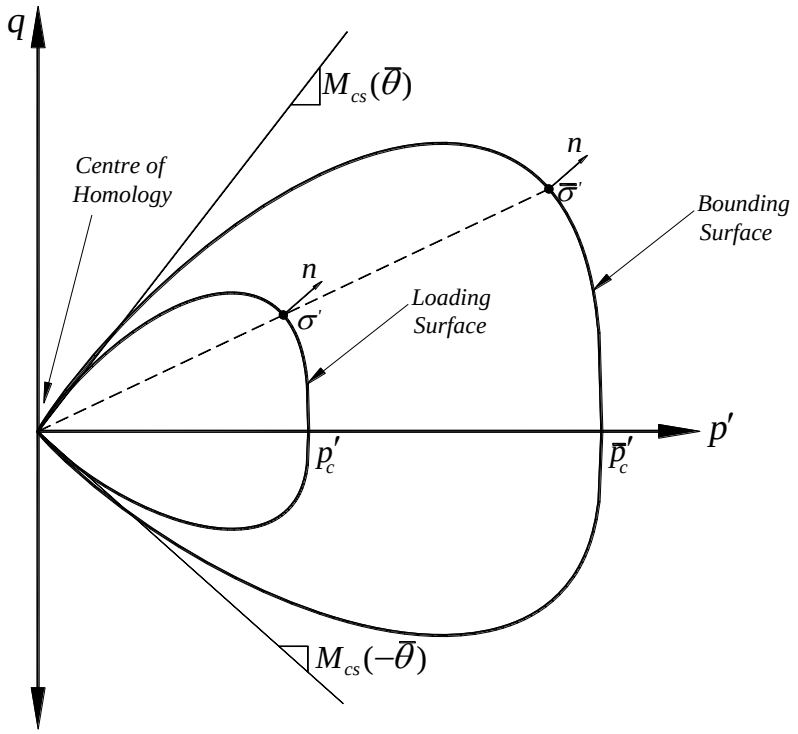

572

573 **Figure 3: Loading surface and mapping rule for first time loading**

574

575

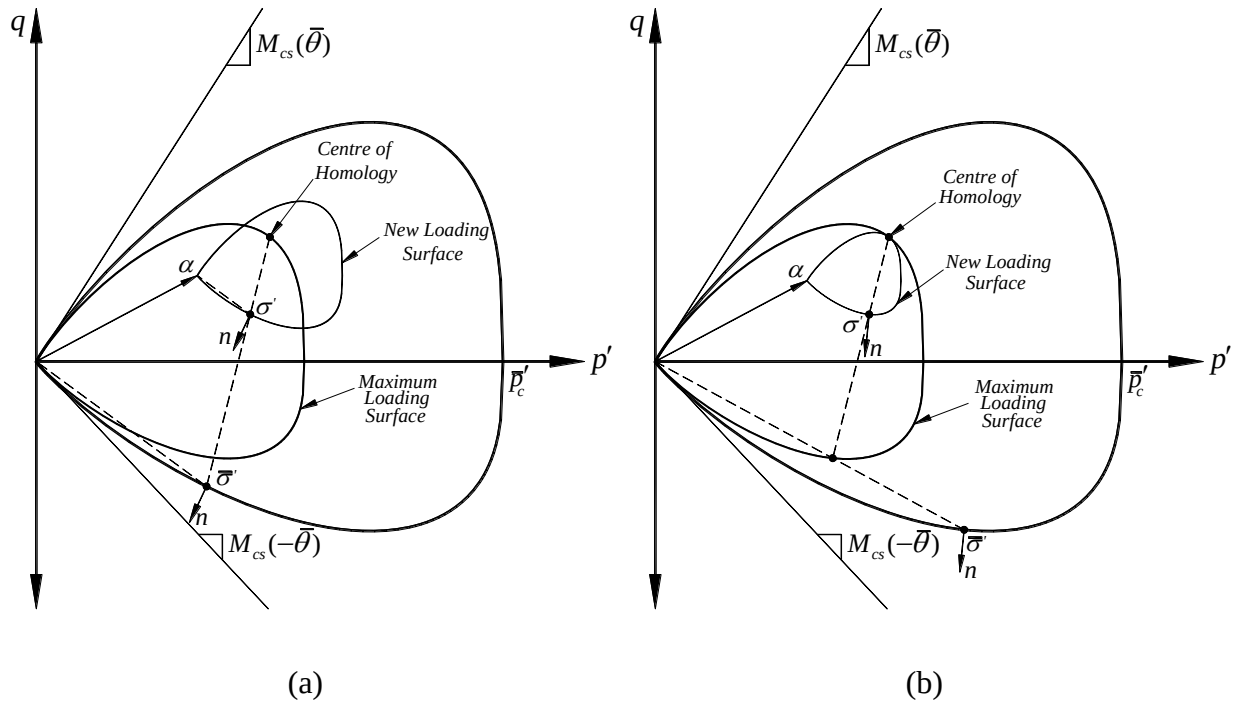

Figure 4: Loading surface and mapping rule for unloading/reloading

(a) current study, (b) Khalili *et al.* (2005)

576

577

578

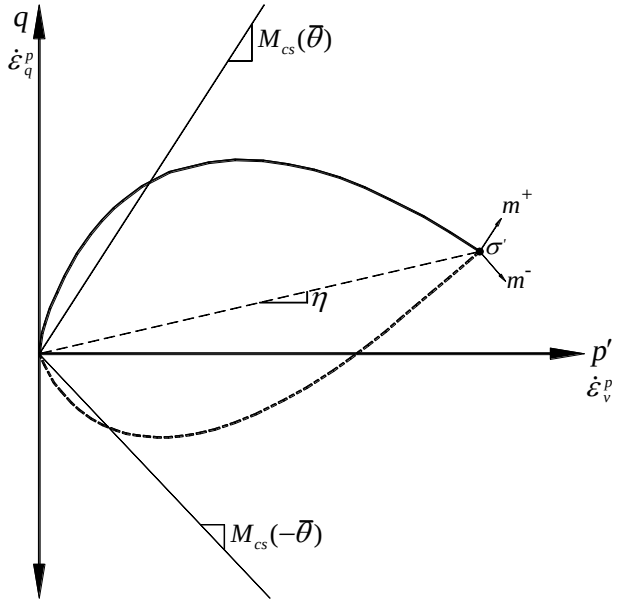

579

580 **Figure 5: Vectors of plastic potential at σ' for compressive and extensive loading**

581

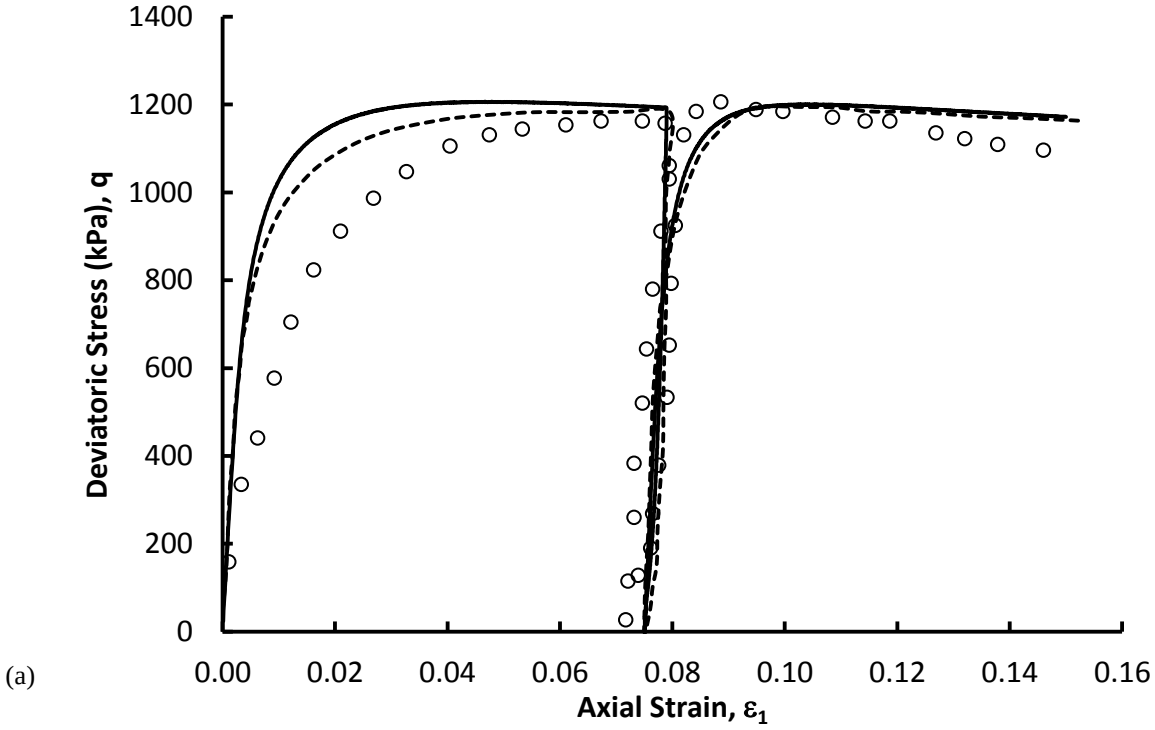

(a)

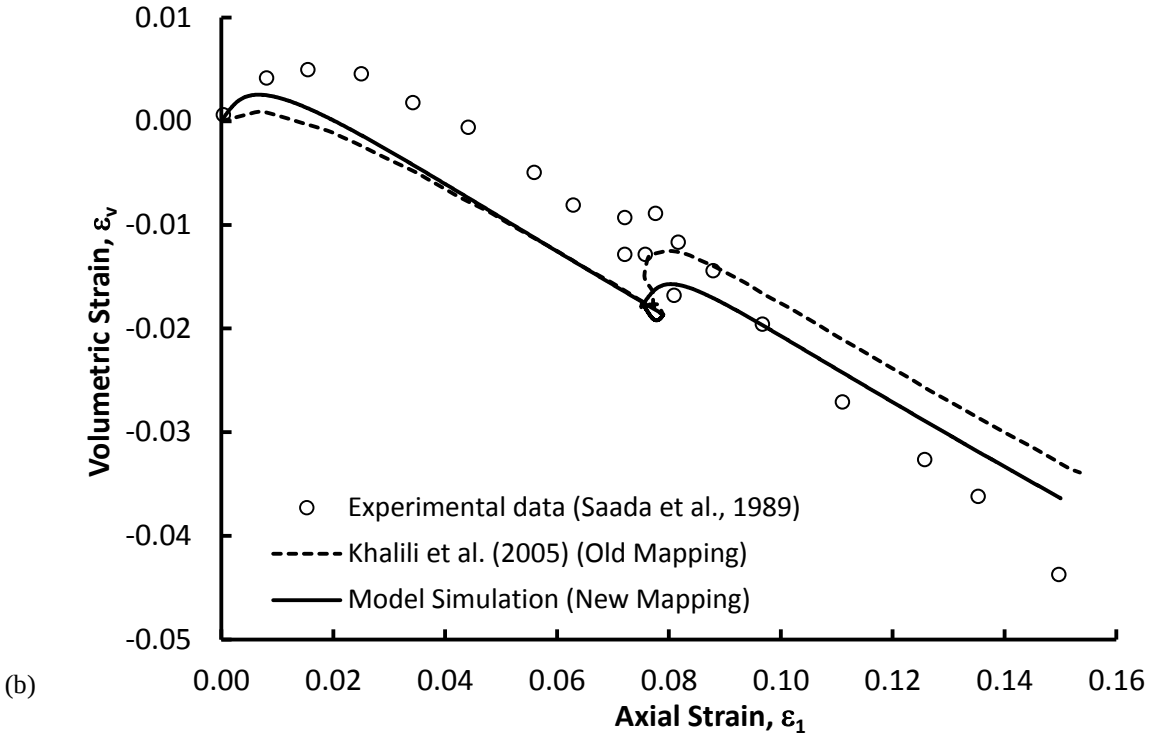

(b)

Figure 6: Drained cyclic test on a dense sample of Hostun sand

(a) $q-\varepsilon_1$ **plot and (b)** $\varepsilon_v-\varepsilon_1$ **plot**

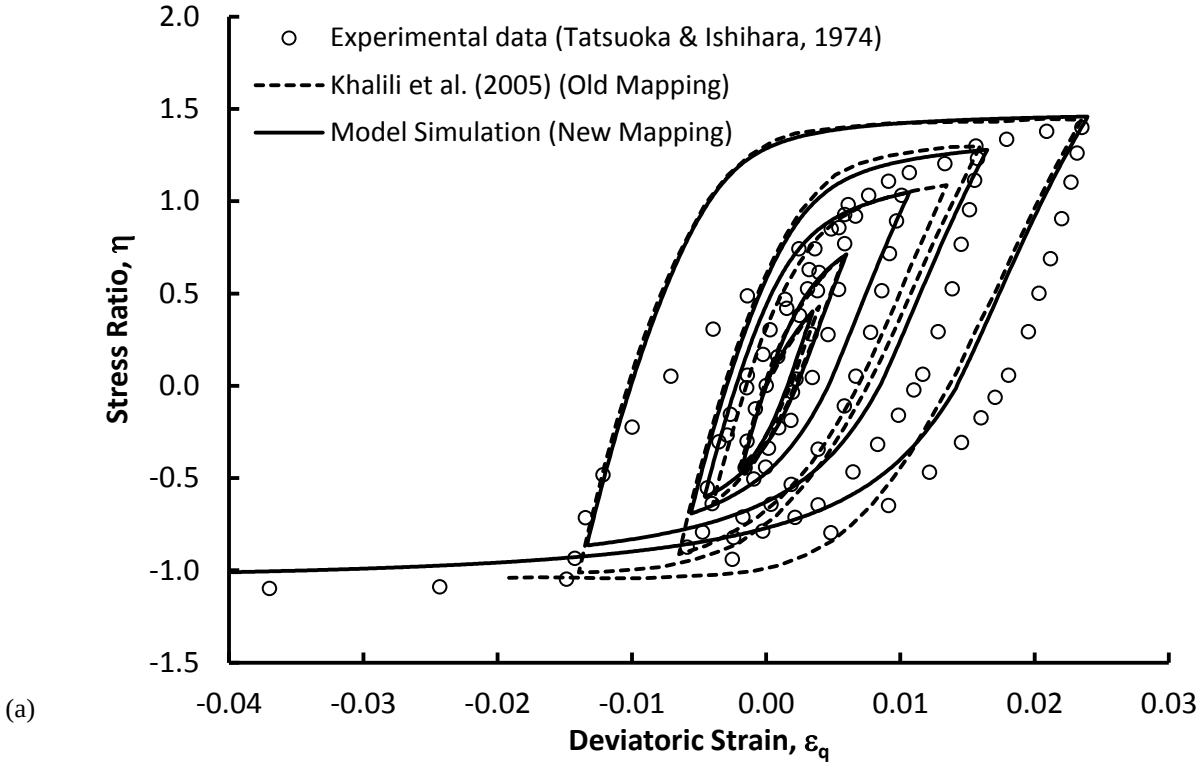

(a)

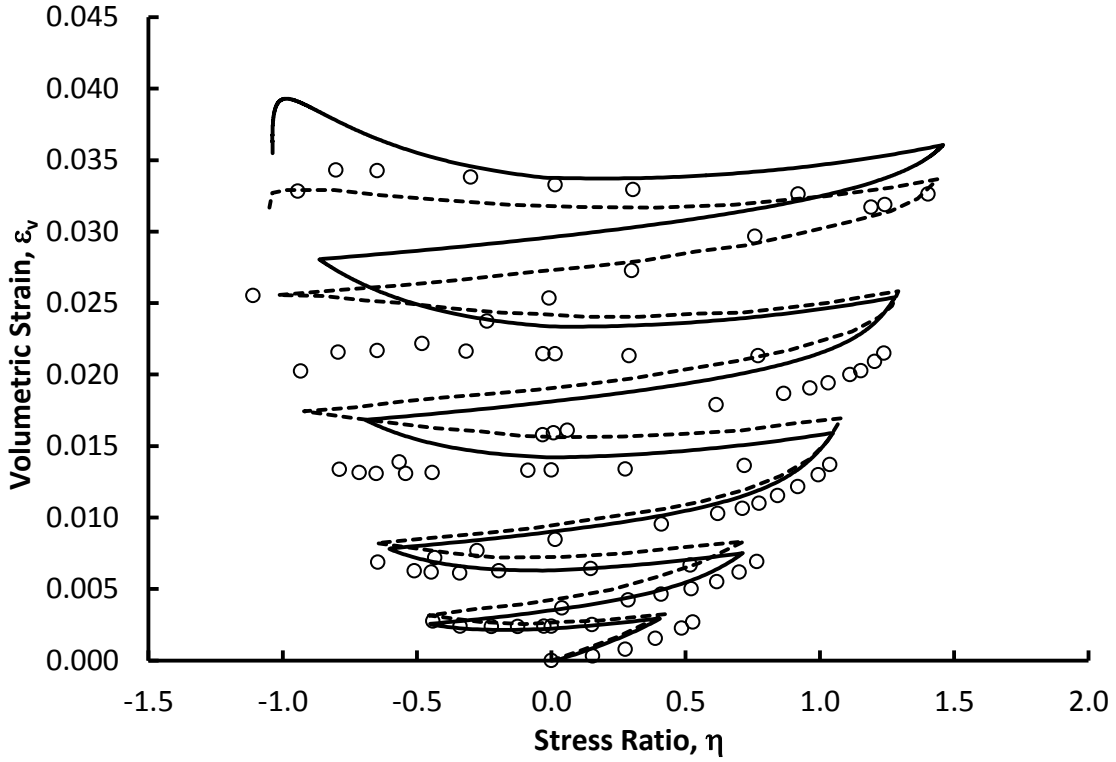

(b)

Figure 7: Drained cyclic test on a loose sample of Fuji River sand

(a) $\eta - \varepsilon_q$ **plot and (b)** $\varepsilon_v - \eta$ **plot**

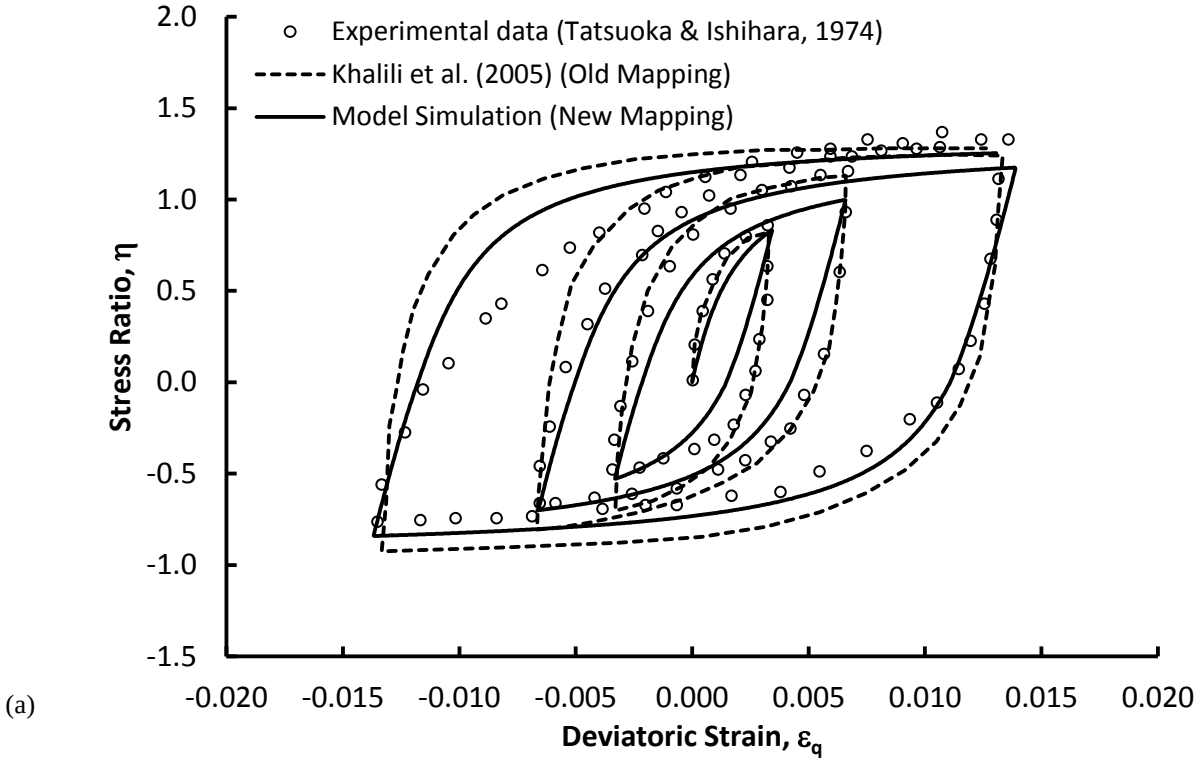

(a)

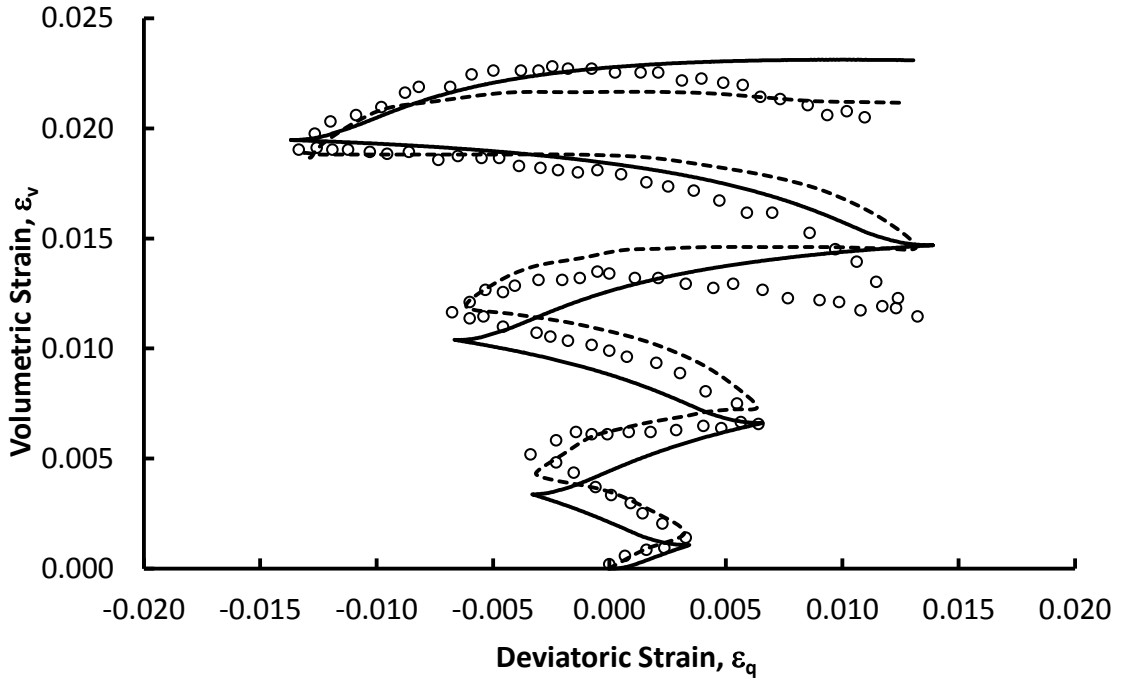

(b)

Figure 8: Drained cyclic test on a loose sample of Toyoura sand

(a) $\eta - \varepsilon_q$ **plot and (b)** $\varepsilon_v - \varepsilon_q$ **plot**

582

583

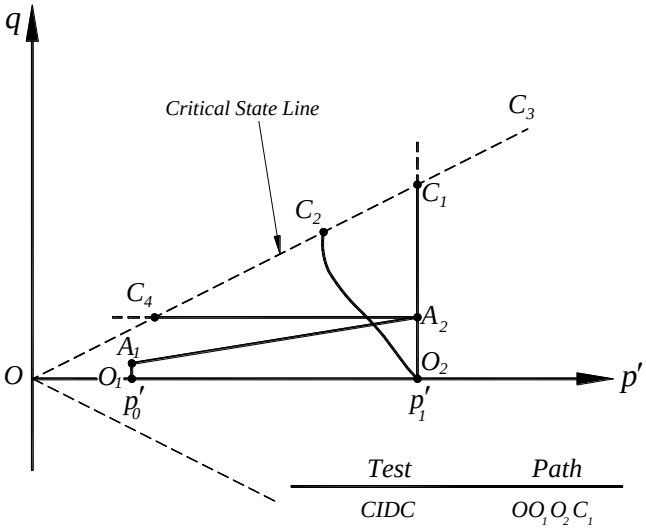

Test	Path
CIDC	$OO_1O_2C_1$
CIUC	$OO_1O_2C_2C_3$
CADC (p'=constant)	$OO_1A_1A_2C_1$
CADC (q=constant)	$OO_1A_1A_2C_4$

584

585 **Figure 9: Stress paths in monotonic tests on Nevada Sand**

586 **(After Arulmoli *et al.*, 1992)**

587

588

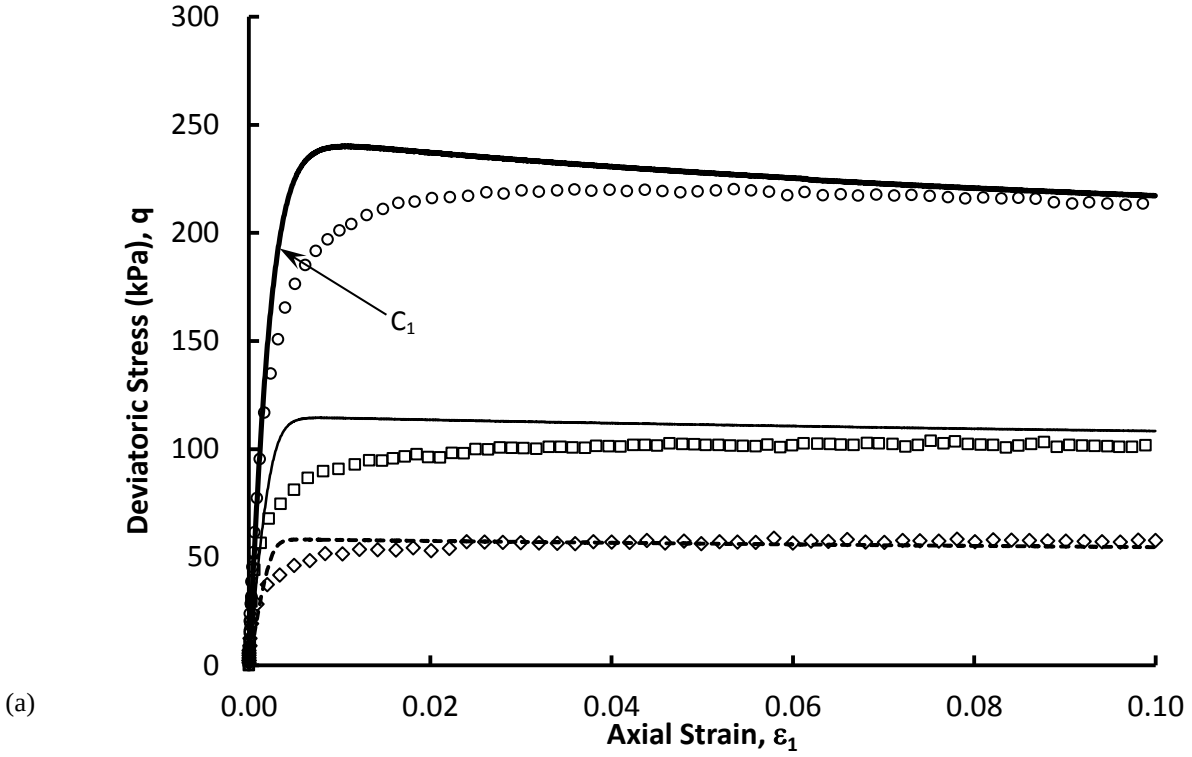

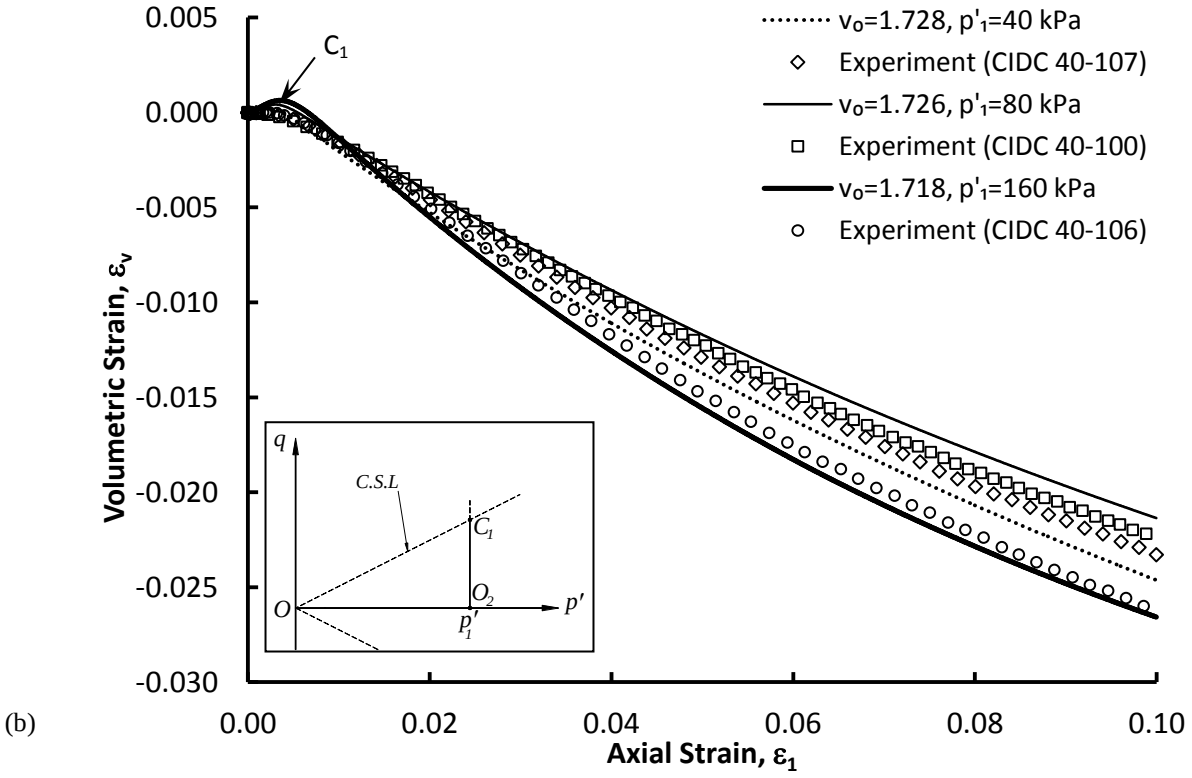

Figure 10: Drained CIDC tests on loose samples of Nevada sand $(D_r = 40\%)$

(a) $q - \varepsilon_1$ **plot and (b)** $\varepsilon_v - \varepsilon_1$ **plot**

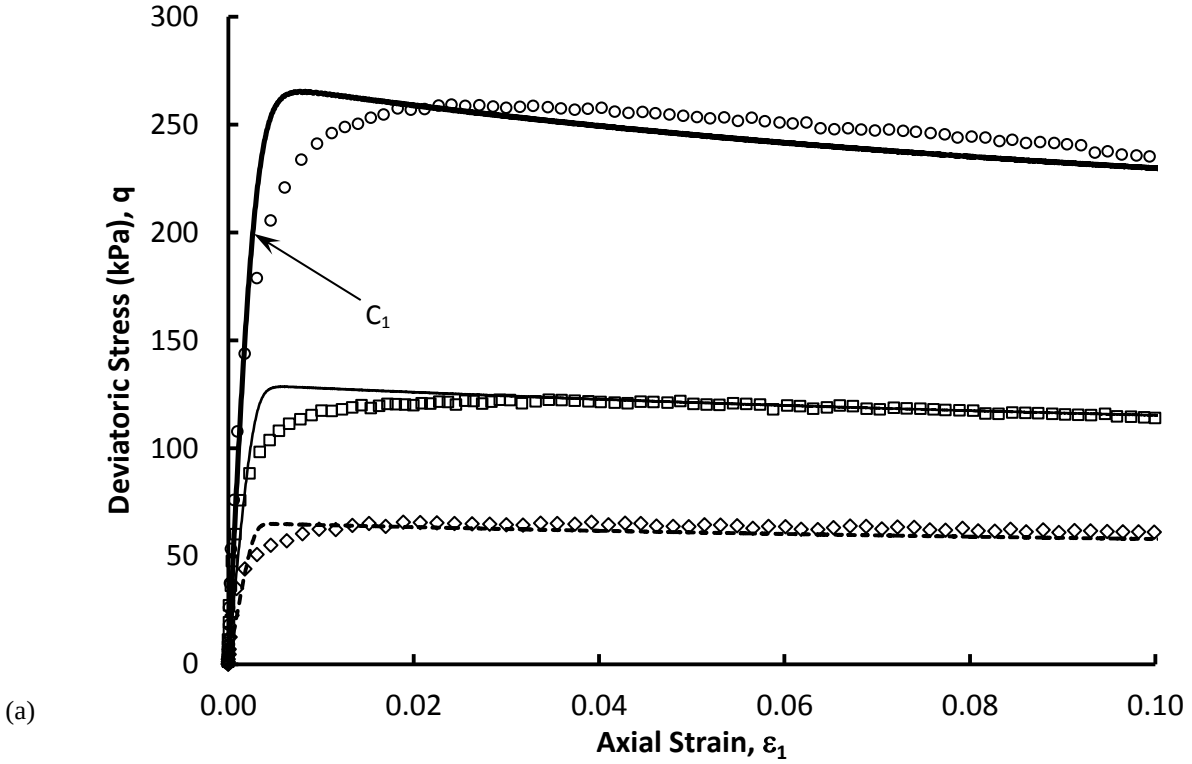

(a)

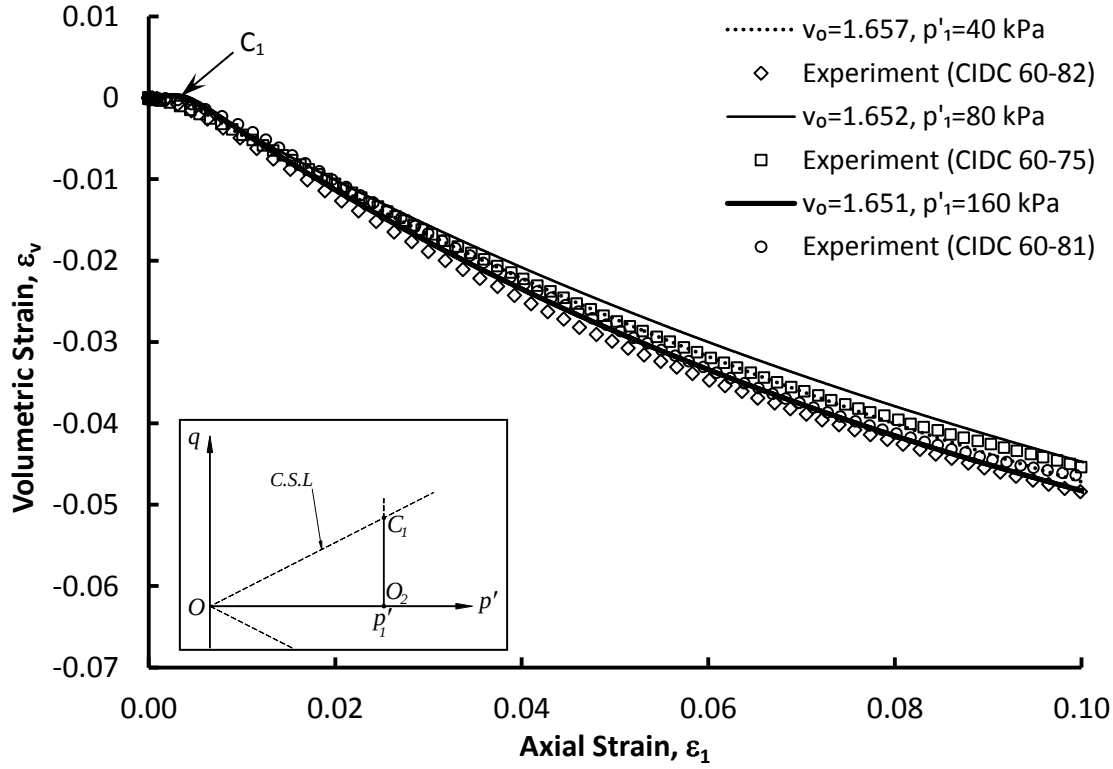

(b)

Figure 11: Drained CIDC tests on dense samples of Nevada sand $(D_r = 60\%)$

(a) $q - \varepsilon_1$ **plot and (b)** $\varepsilon_v - \varepsilon_1$ **plot**

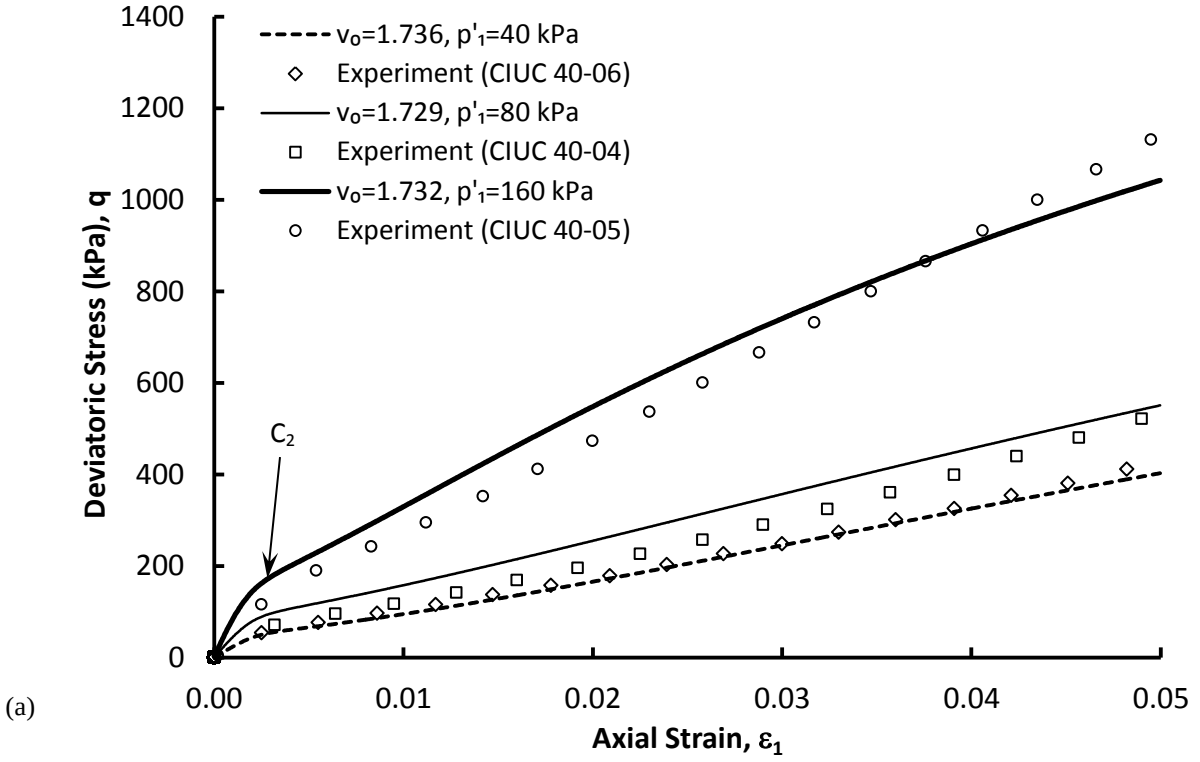

(a)

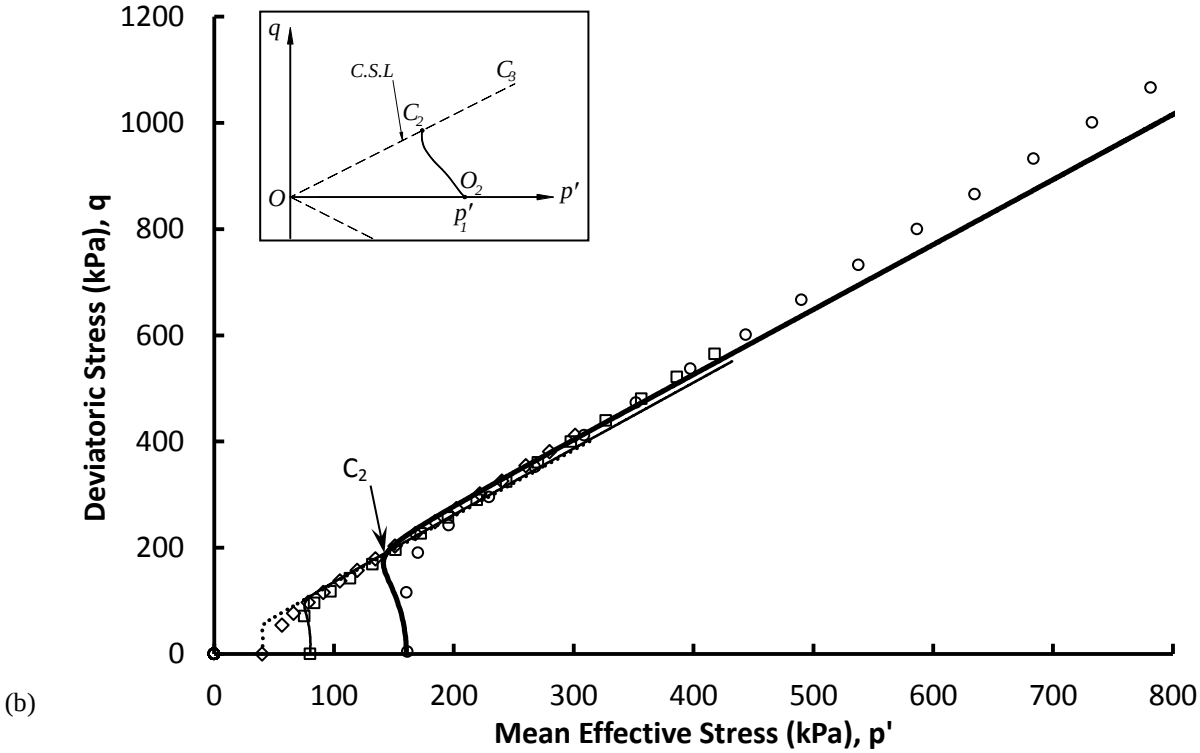

(b)

Figure 12: Undrained CIUC tests on loose samples of Nevada sand $(D_r = 40\%)$

(a) $q - \varepsilon_1$ **plot and (b)** $q - p'$ **plot**

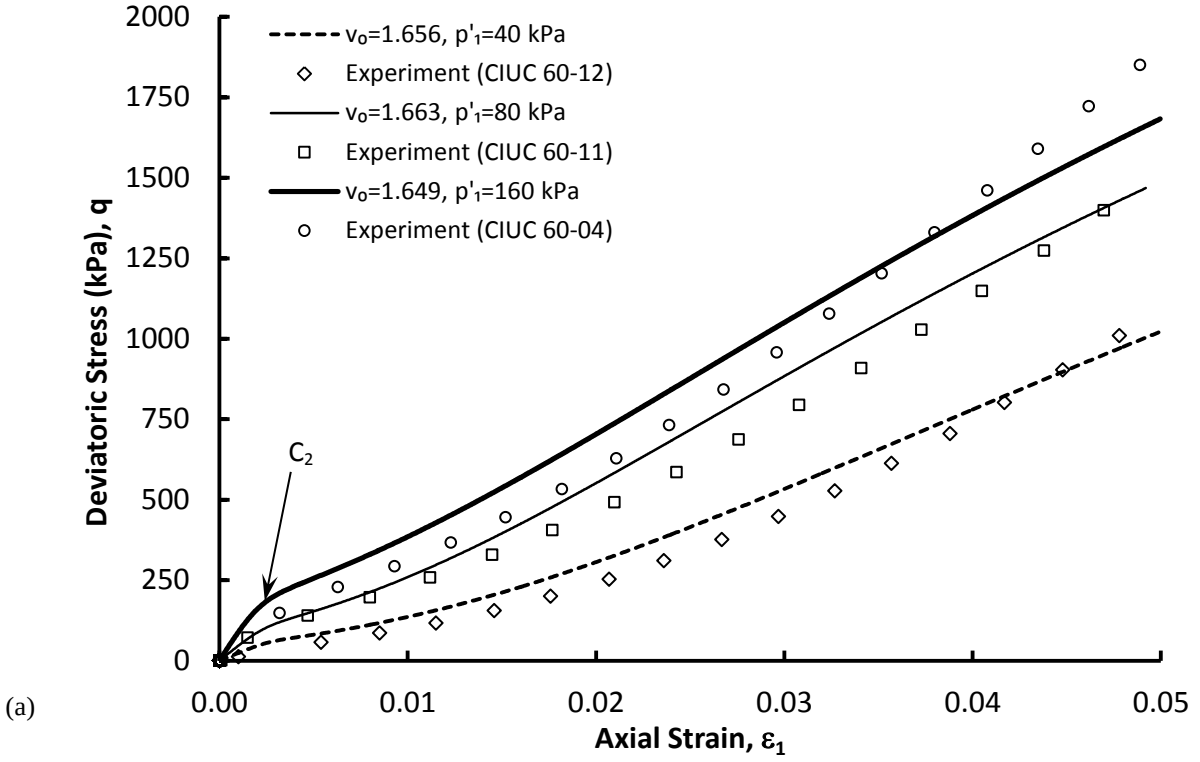

(a)

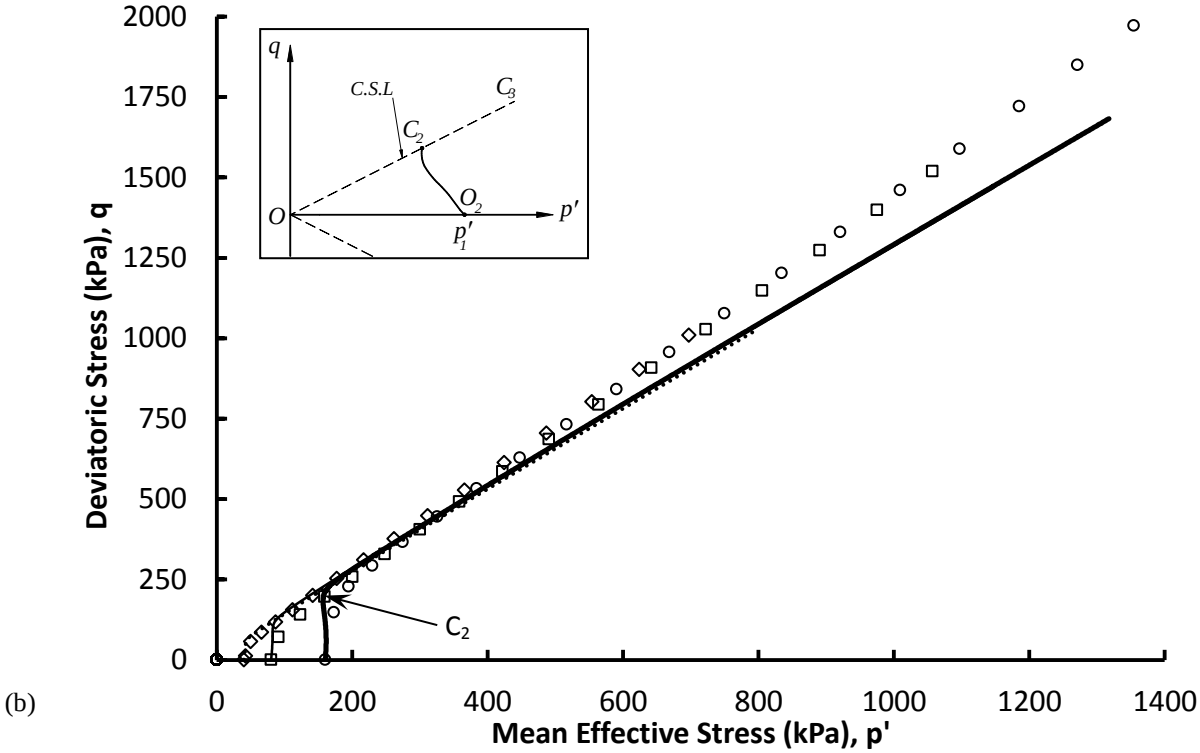

(b)

Figure 13: Undrained CIUC tests on dense samples of Nevada sand $(D_r = 60\%)$

(a) $q - \varepsilon_1$ **plot and (b)** $q - p'$ **plot**

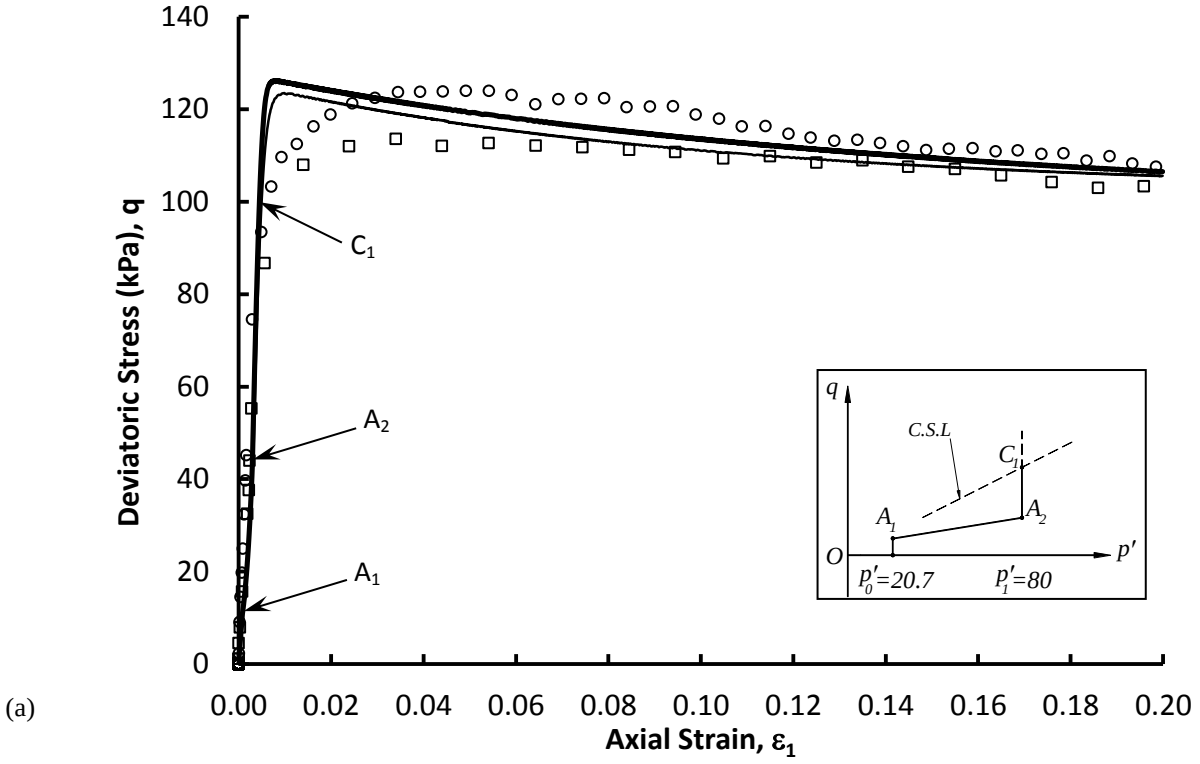

(a)

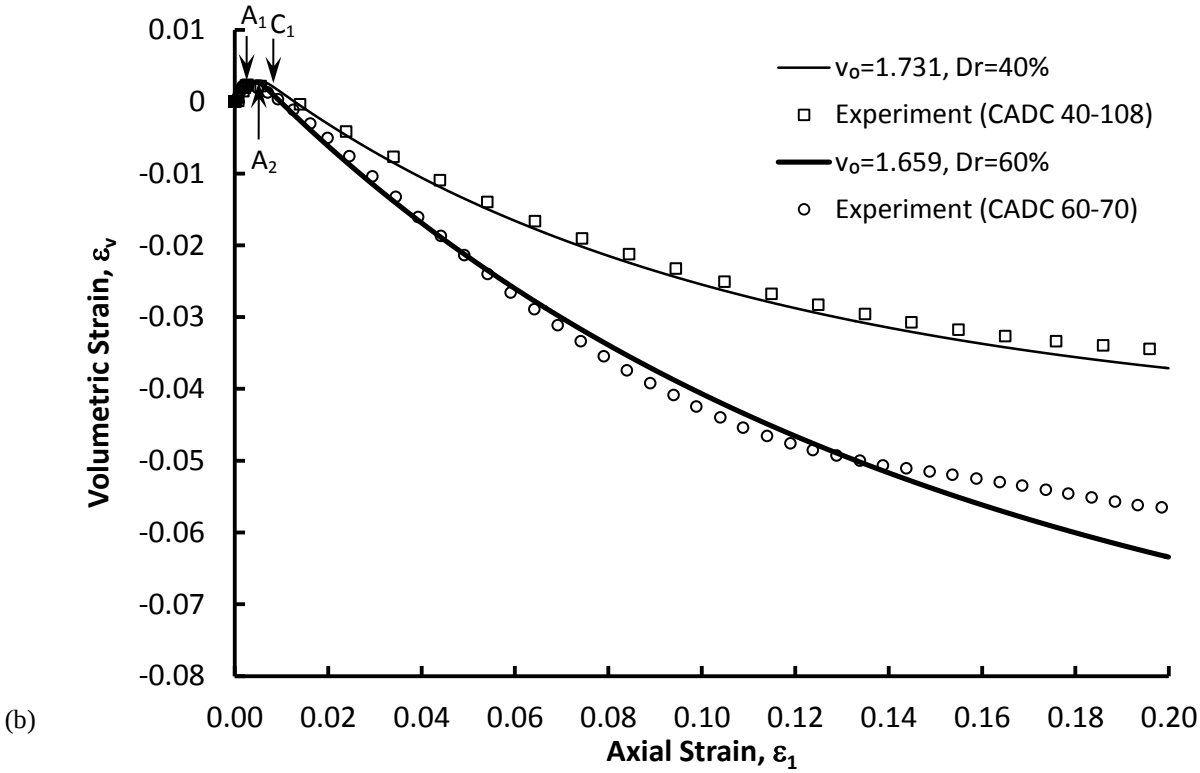

(b)

Figure 14: Drained CADC tests with constant p' on Nevada sand

(a) $q-\varepsilon_1$ plot and (b) $\varepsilon_v-\varepsilon_1$ plot

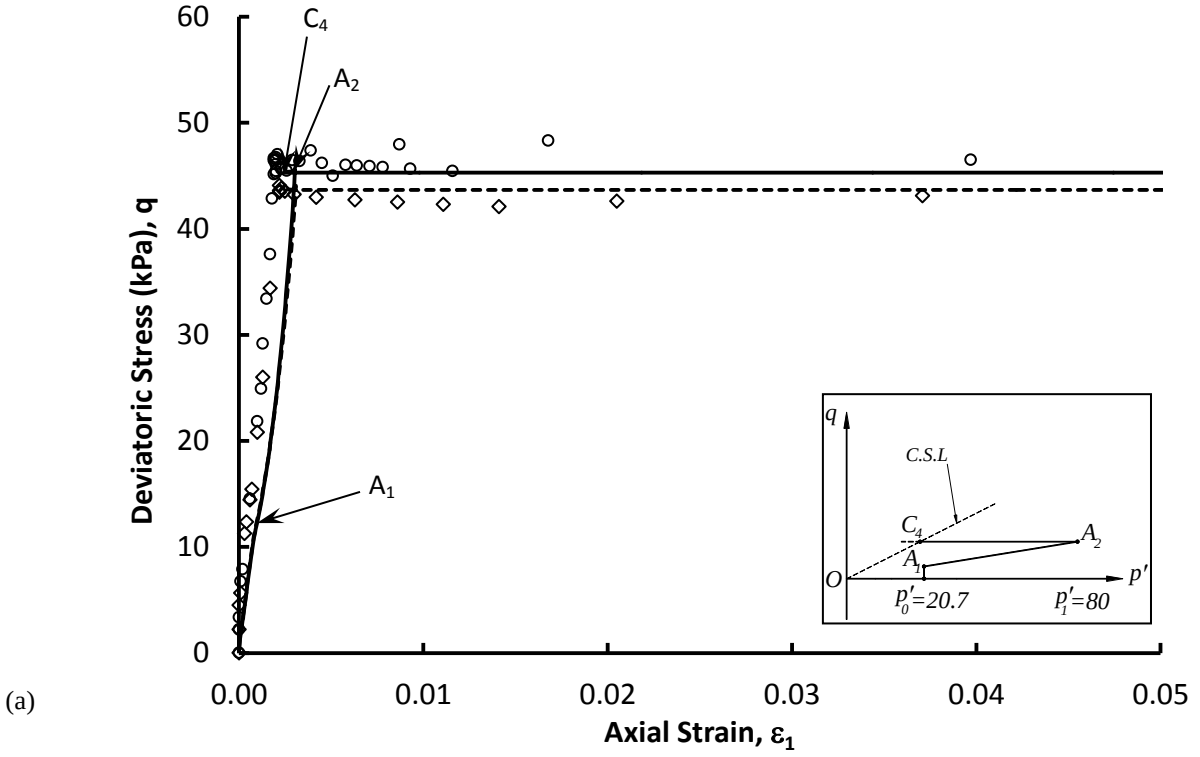

(a)

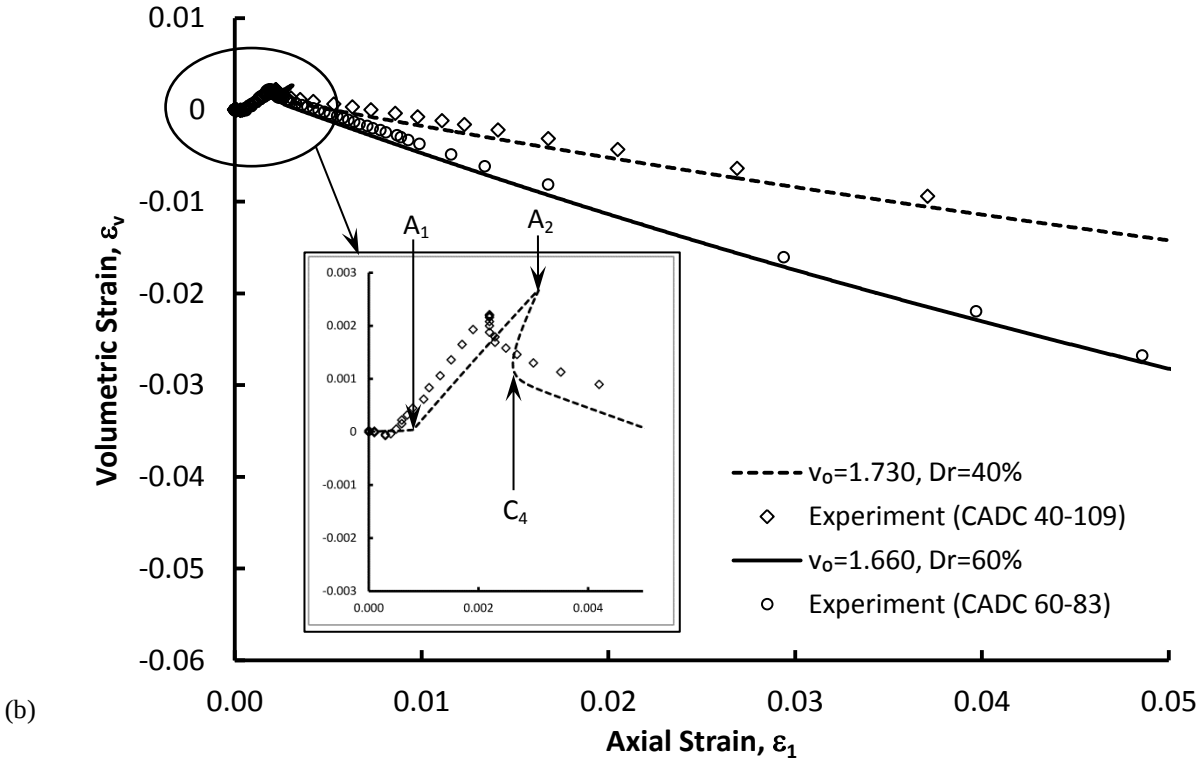

(b)

Figure 15: Drained CADC tests with constant q on Nevada sand

(a) $q-\varepsilon_1$ plot and (b) $\varepsilon_v-\varepsilon_1$ plot

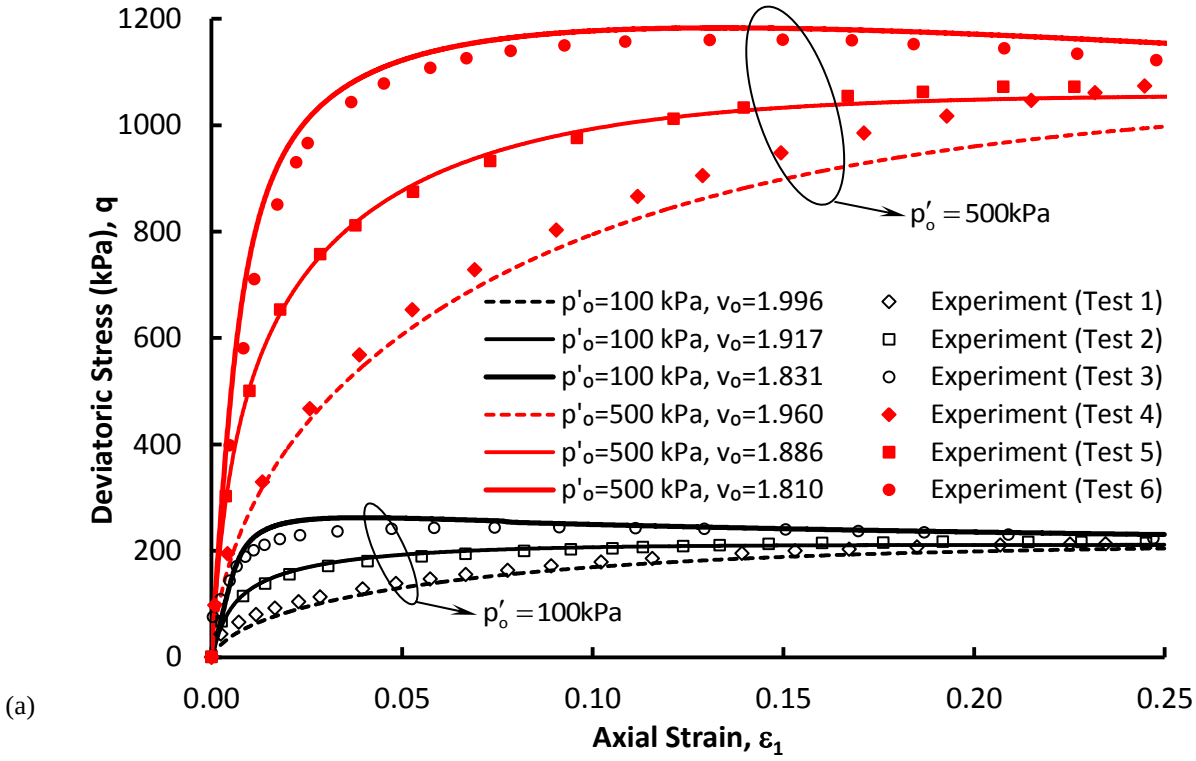

(a)

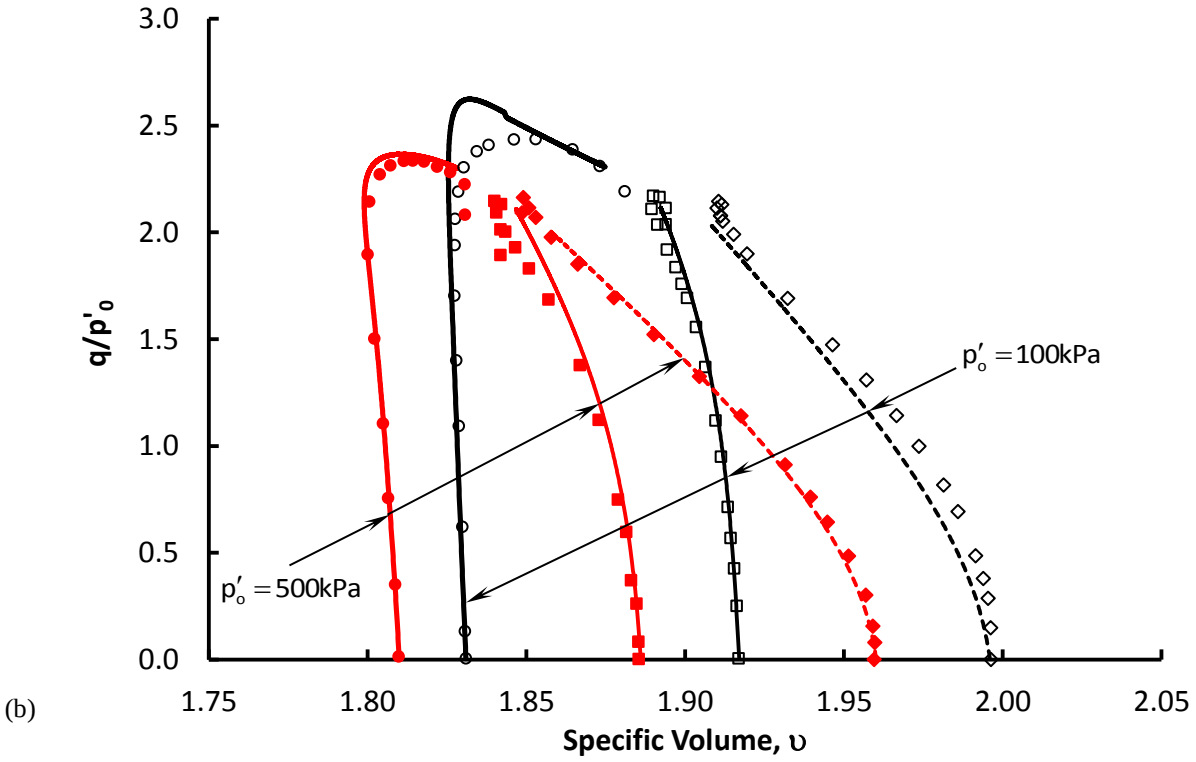

(b)

Figure 16: Drained tests on Toyoura sand

(a) $q-\varepsilon_1$ **plot and (b)** $q/p_0'-\upsilon$ **plot**

589

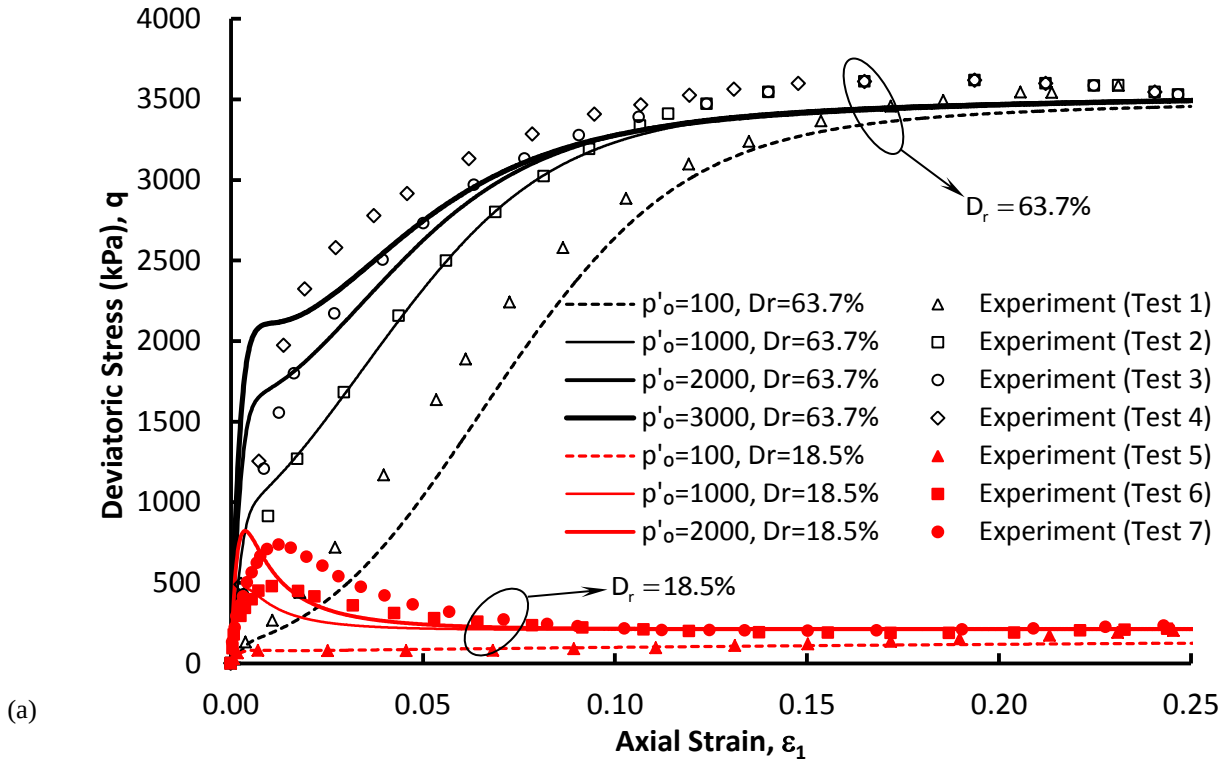

(a)

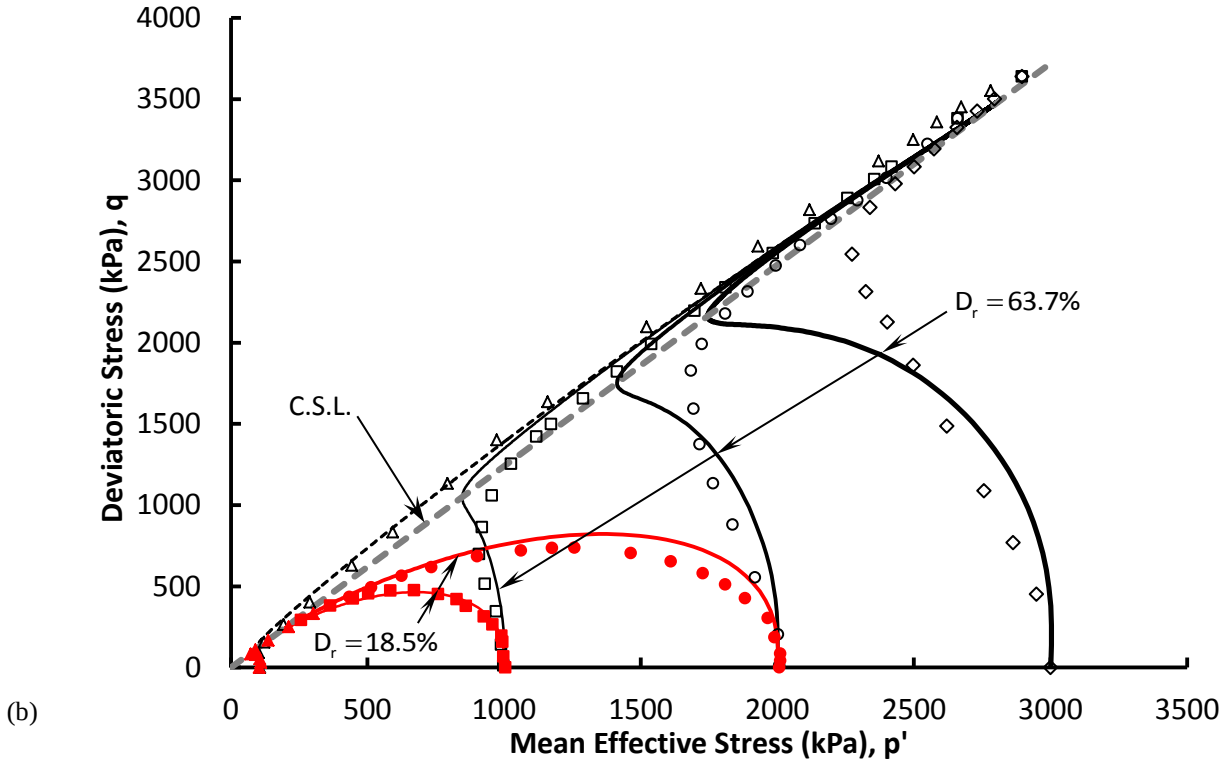

(b)

Figure 17: Undrained tests on Toyoura sand

(a) $q-\varepsilon_1$ **plot and (b)** $q-p'$ **plot**

590

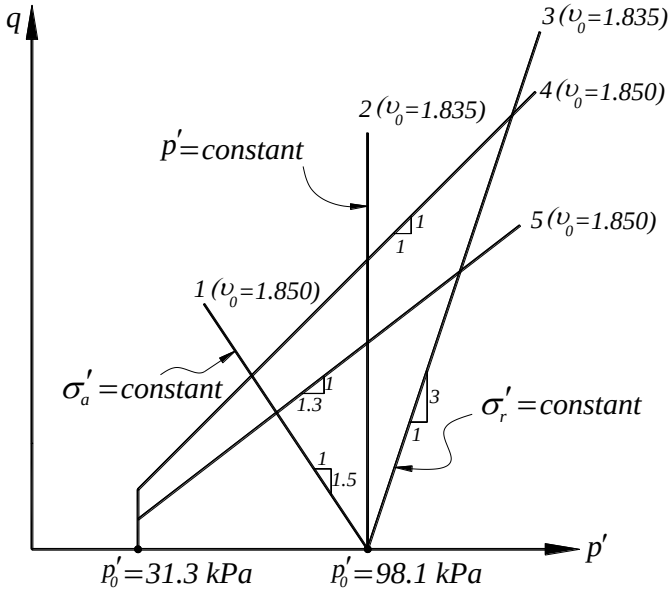

Figure 18: Stress paths used for tests on Toyoura sand (Pradhan *et al.*, 1989a)

(a)

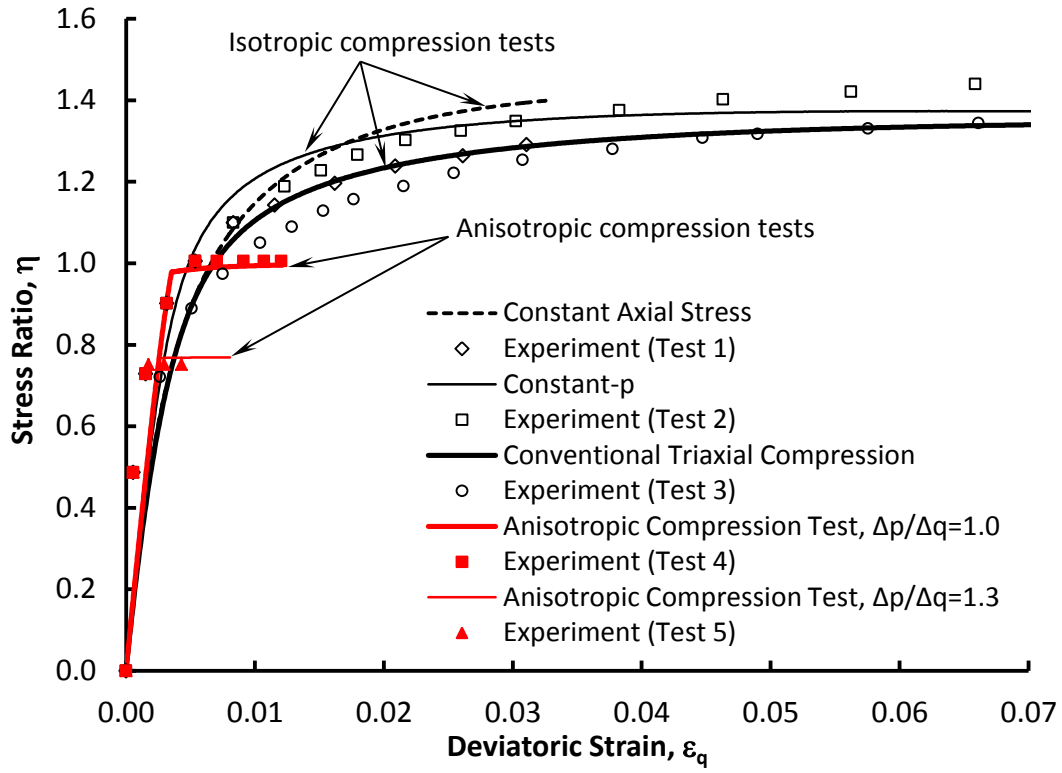

(b)

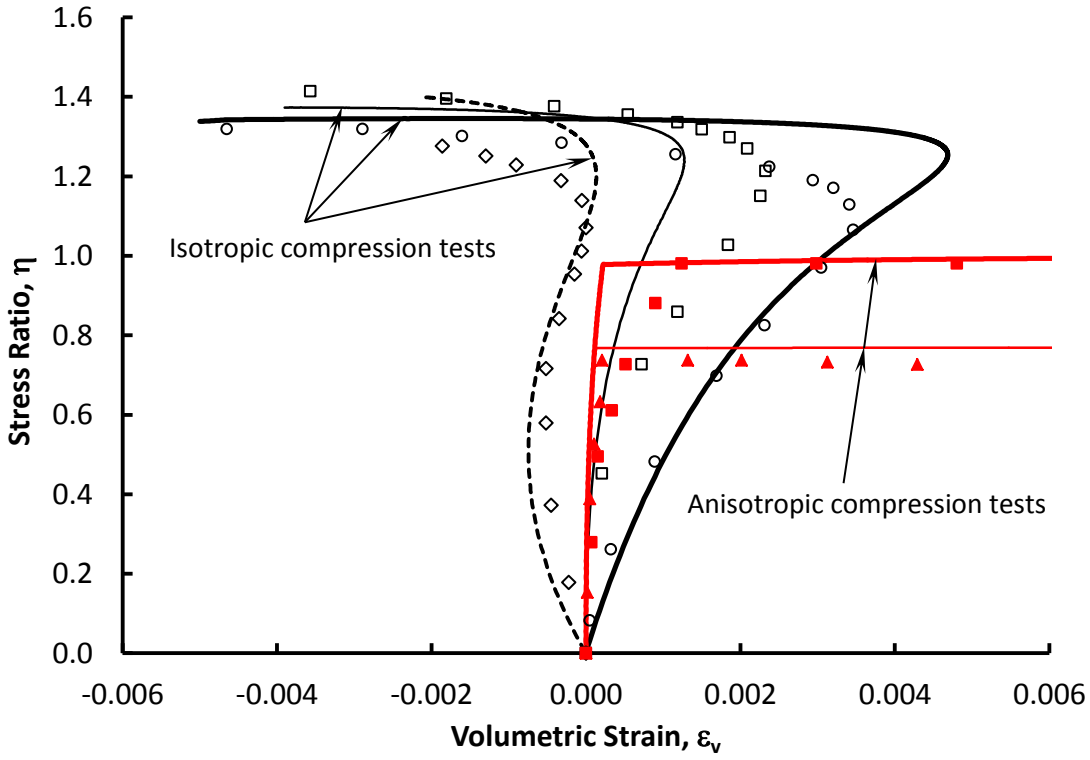

Figure 19: Drained tests with various stress paths on Toyoura sand

(a) $\eta - \varepsilon_q$ **plot and (b)** $\eta - \varepsilon_v$ **plot**

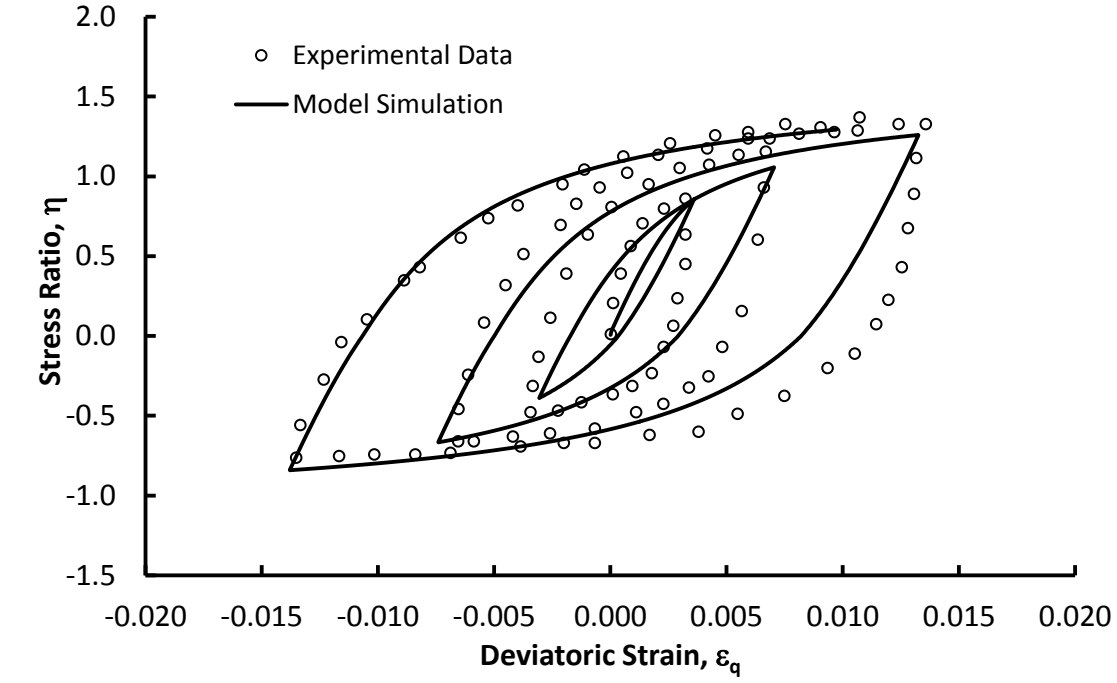

(a)

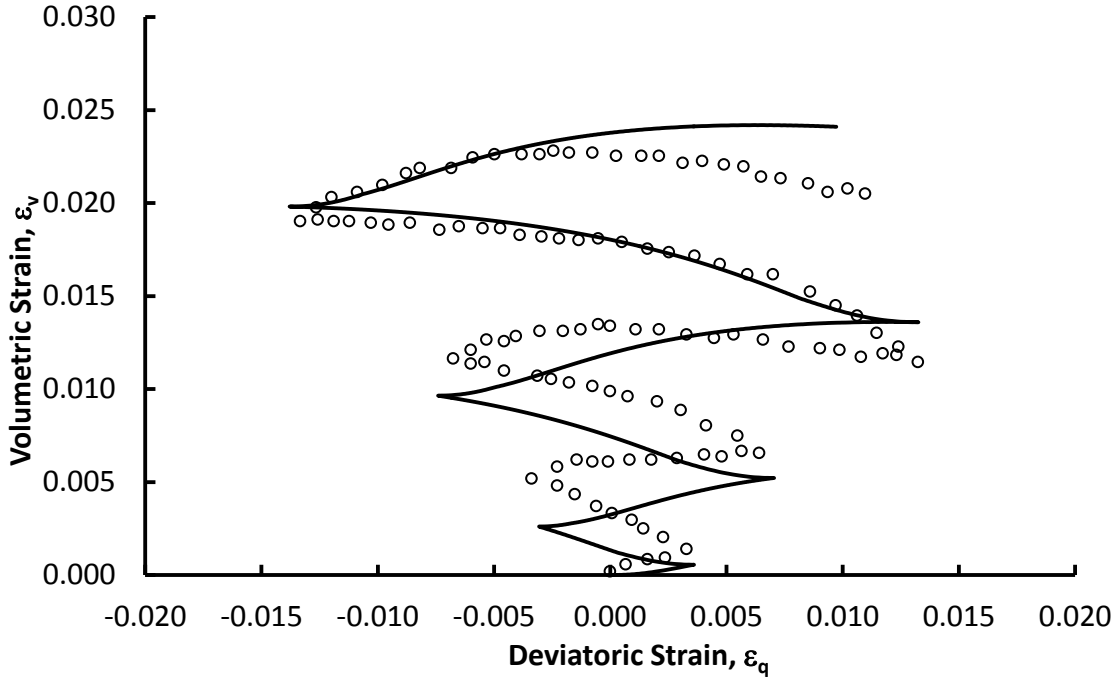

(b)

Figure 20: Drained cyclic test on a loose sample of Toyoura sand with increasing shear strain amplitude

(a) $\eta - \varepsilon_q$ **plot and (b)** $\varepsilon_v - \varepsilon_q$ **plot**

594

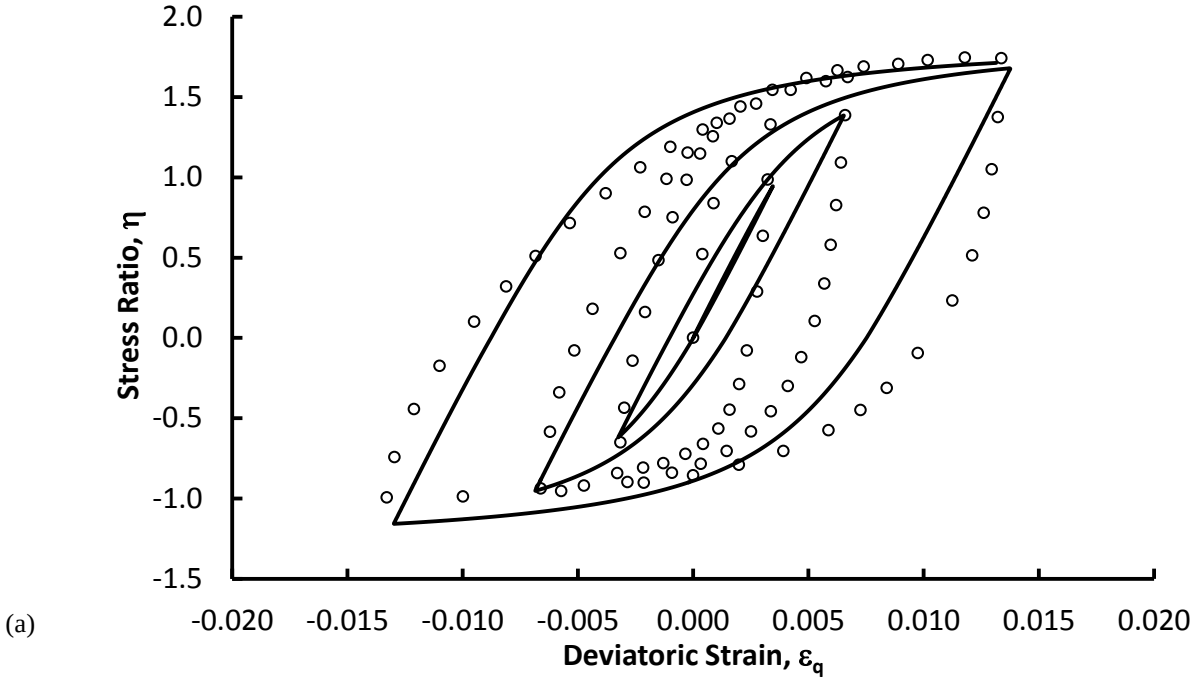

(a)

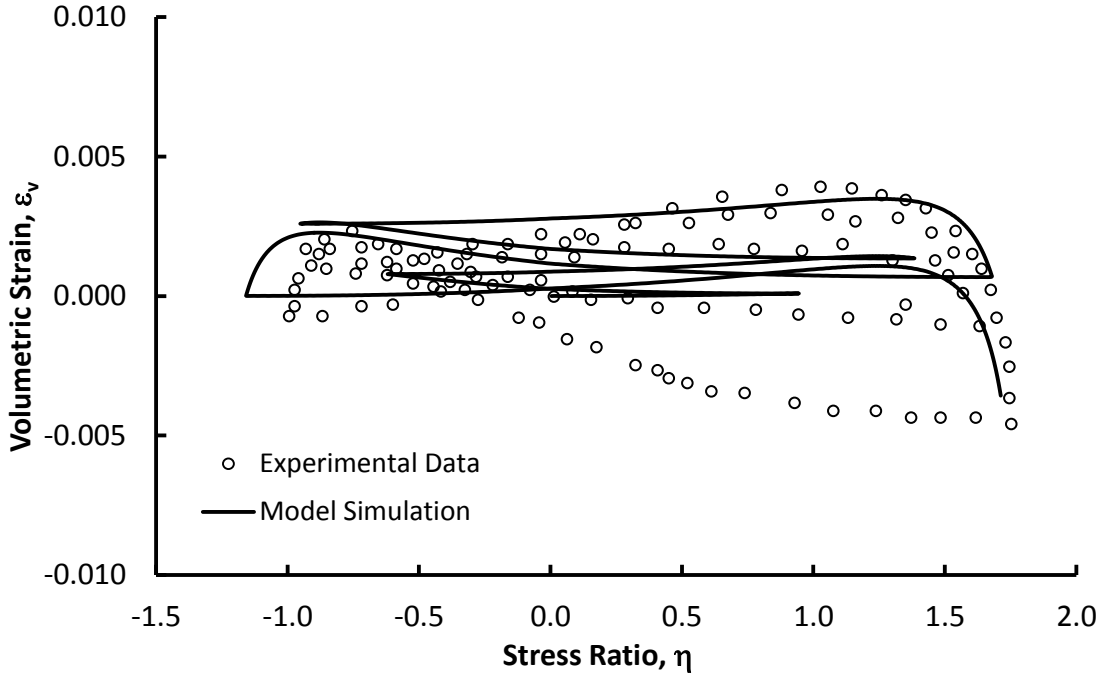

(b)

Figure 21: Drained cyclic test on a dense sample of Toyoura sand with increasing shear strain amplitude

(a) $\eta - \varepsilon_q$ **plot and (b)** $\varepsilon_v - \eta$ **plot**

595

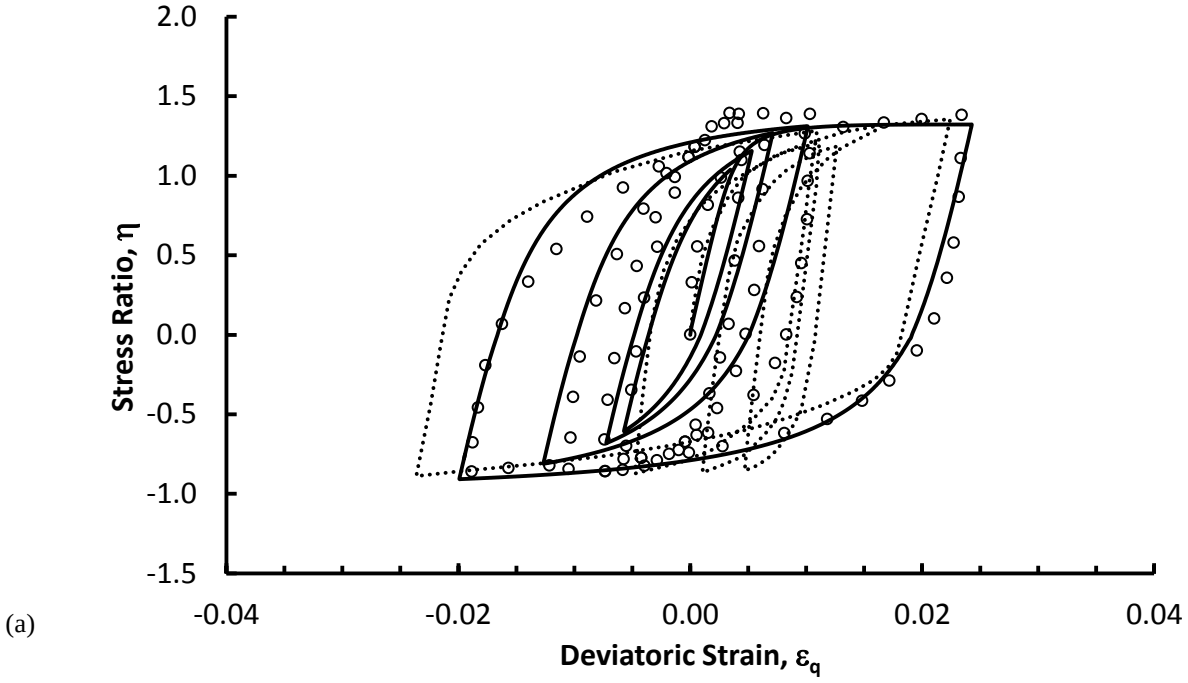

(a)

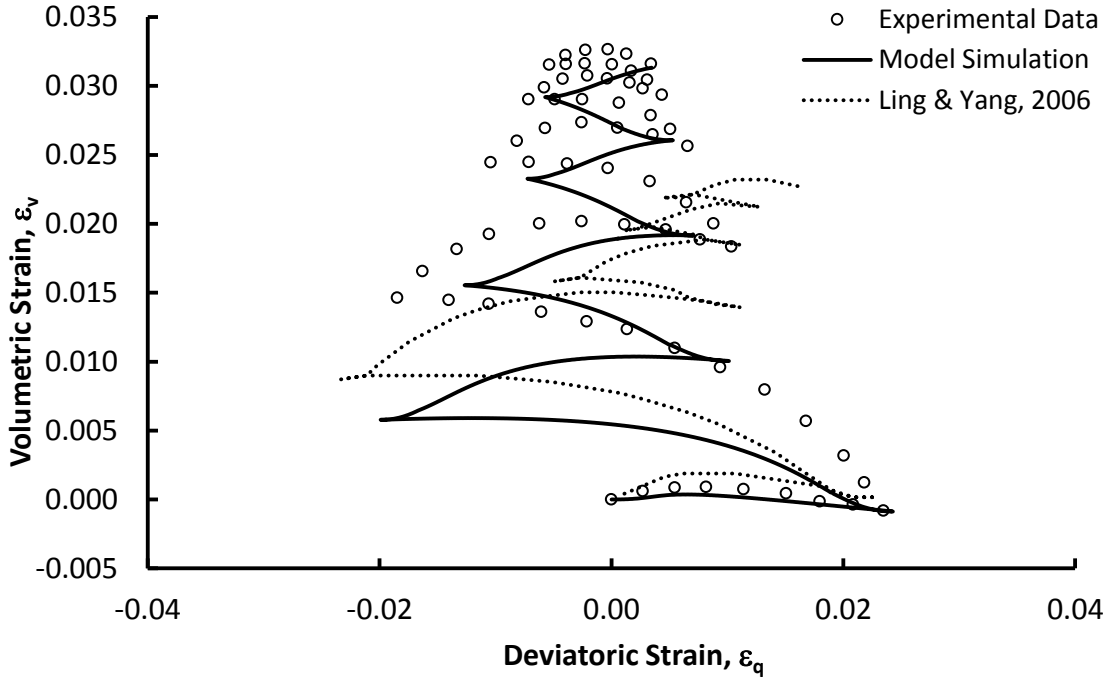

(b)

Figure 22: Drained cyclic test on a very loose sample of Toyoura sand with decreasing shear strain amplitude

(a) $\eta - \varepsilon_q$ **plot and (b)** $\varepsilon_v - \varepsilon_q$ **plot**

596

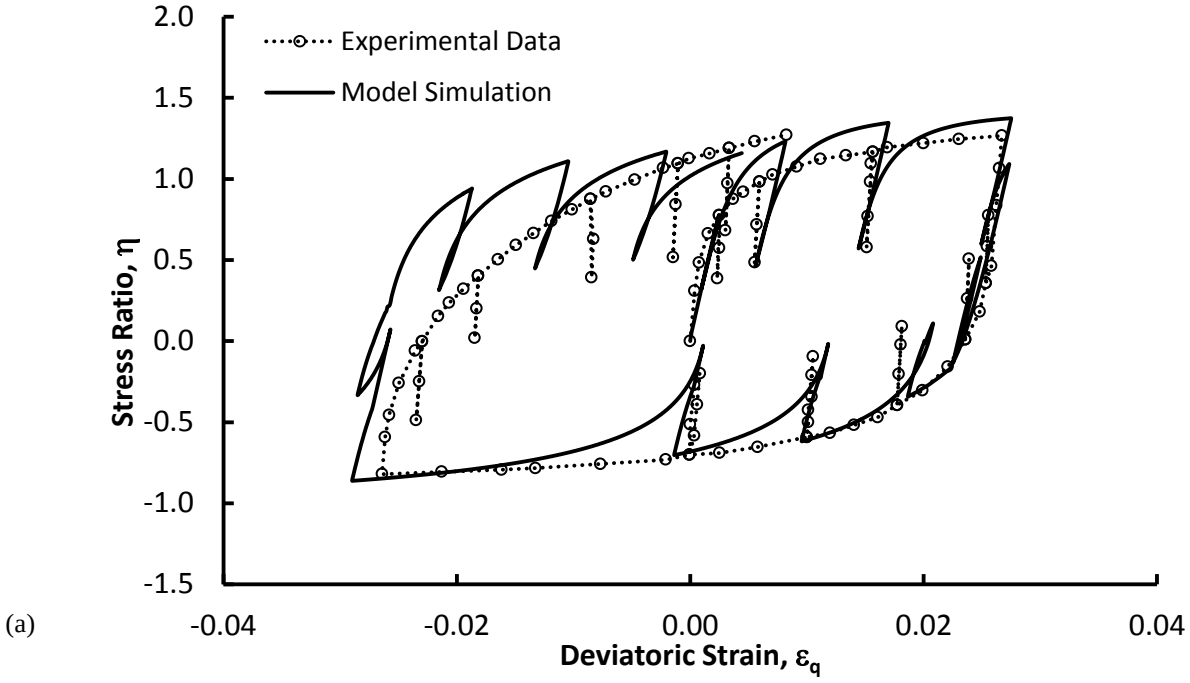

(a)

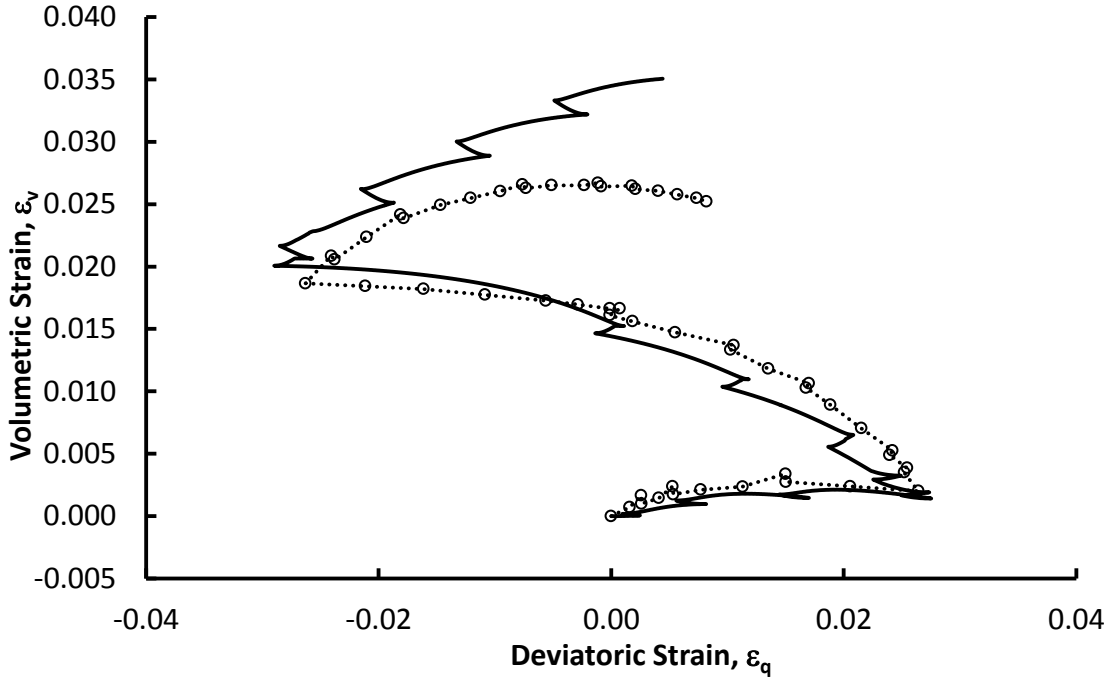

(b)

Figure 23: Drained cyclic test on a very loose sample of Toyoura sand with small hysteresis loops

(a) $\eta - \varepsilon_q$ **plot and (b)** $\varepsilon_v - \varepsilon_q$ **plot**

597

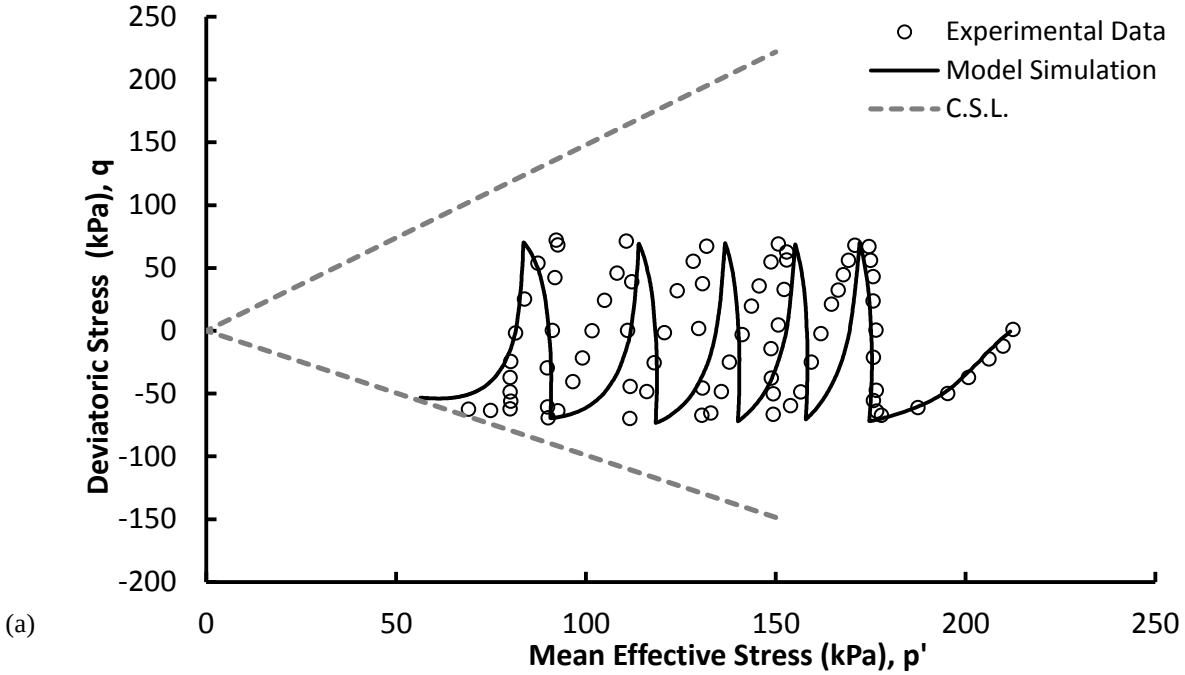

(a)

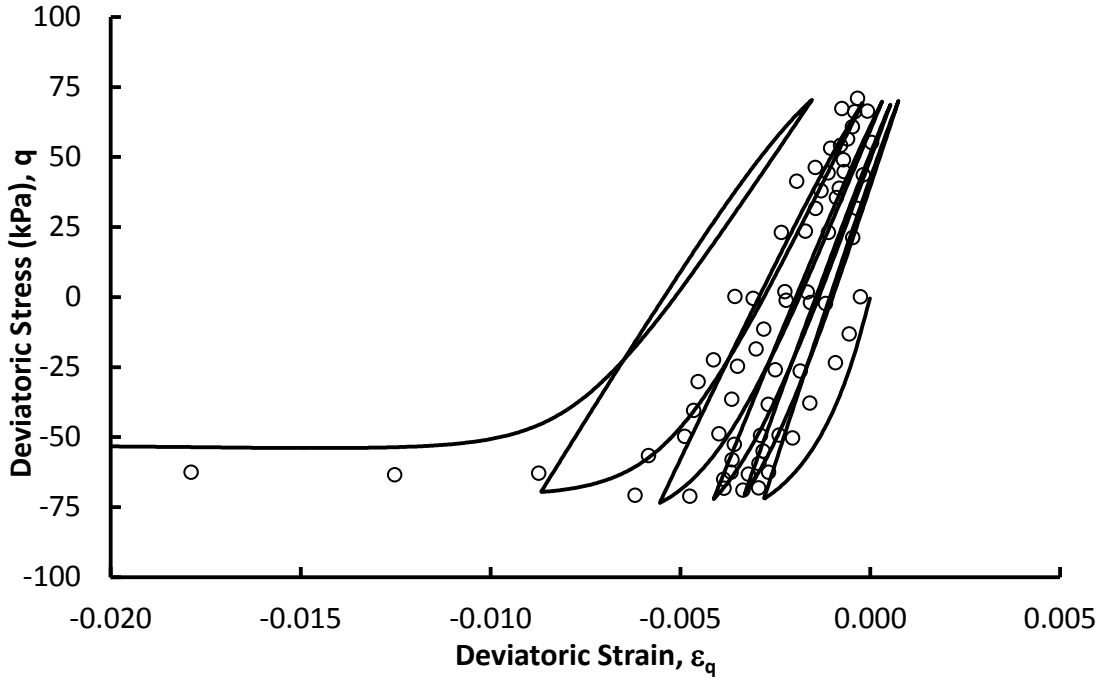

(b)

Figure 24: Undrained cyclic test with constant cyclic amplitude on a loose sample of Fuji River sand

(a) $q - p'$ **plot and (b)** $q - \varepsilon_q$ **plot**

598

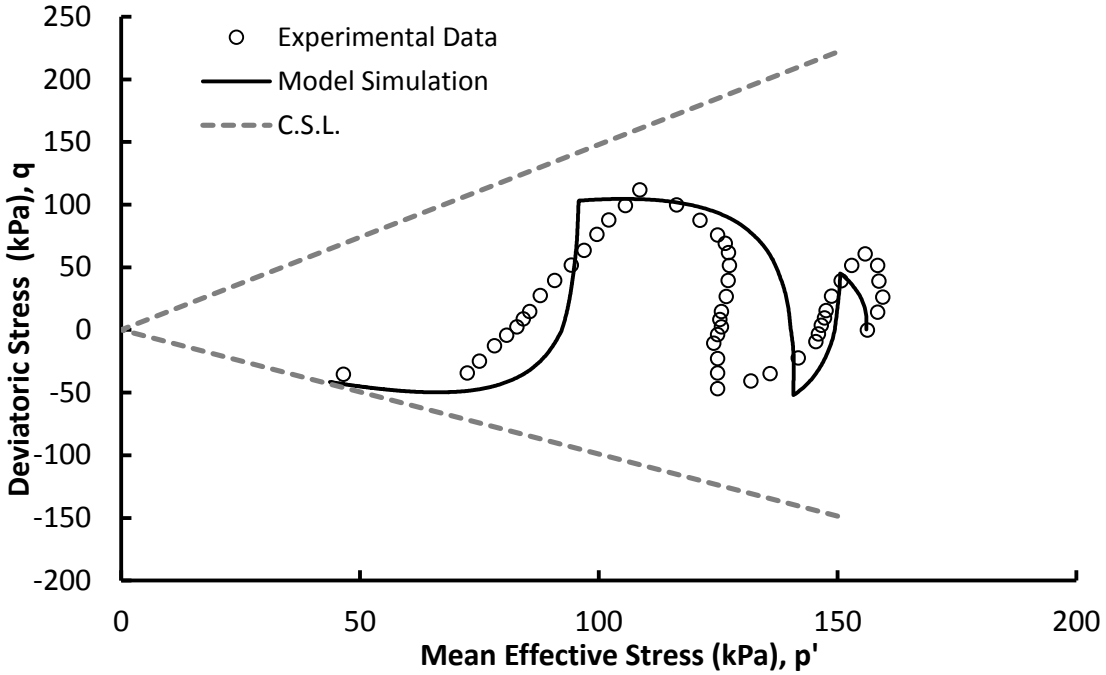

(a)

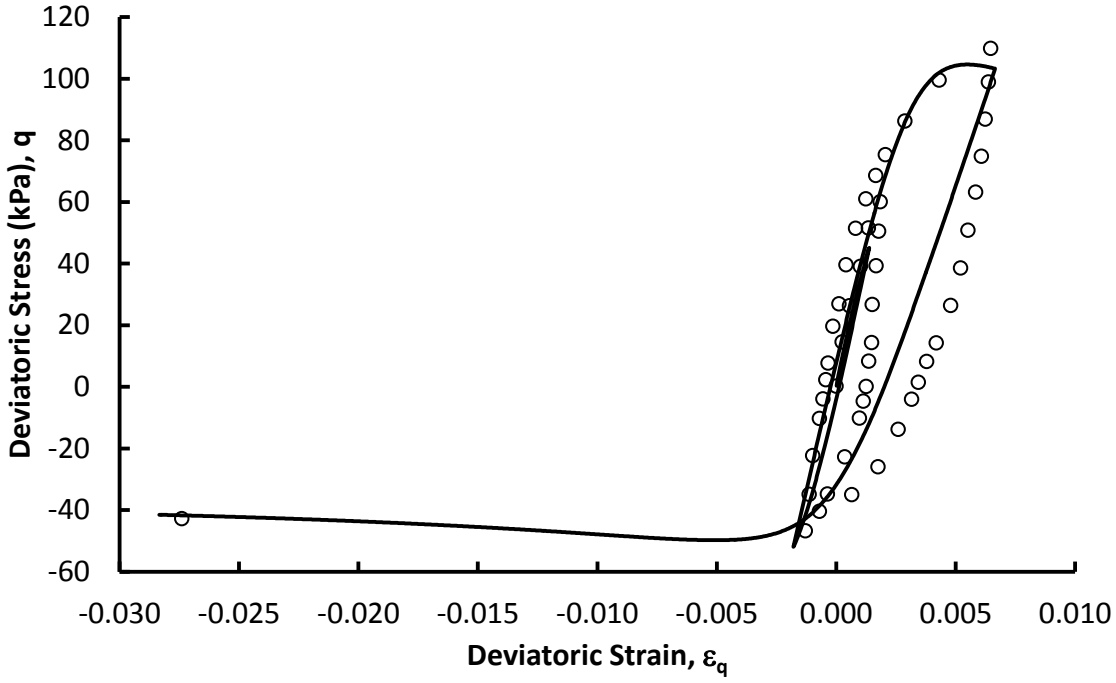

(b)

Figure 25: Undrained cyclic test with irregular cyclic amplitude on a loose sample of Fuji River sand

(a) $q - p'$ **plot and (b)** $q - \varepsilon_q$ **plot**

599

600 **List of Figure Captions**

601 Figure 1: Critical State Line (CSL) and Limiting Isotropic Compression Line (LICL)

602 Figure 2: Effect of N and R on the shape of the bounding surface in $p' - q - \theta$ space

603 Figure 3: Loading surface and mapping rule for first time loading

604 Figure 4: Loading surface and mapping rule for unloading/reloading

605 Figure 5: Vectors of plastic potential at $\boldsymbol{\sigma}'$ for compressive and extensive loading

606 Figure 6: Drained cyclic test on a dense sample of Hostun sand

607 Figure 7: Drained cyclic test on a loose sample of Fuji River sand

608 Figure 8: Drained cyclic test on a loose sample of Toyoura sand

609 Figure 9: Stress paths in monotonic tests on Nevada Sand

610 Figure 10: Drained CIDC tests on loose samples of Nevada sand ($D_r = 40\%$)

611 Figure 11: Drained CIDC tests on dense samples of Nevada sand ($D_r = 60\%$)

612 Figure 12: Undrained CIUC tests on loose samples of Nevada sand ($D_r = 40\%$)

613 Figure 13: Undrained CIUC tests on dense samples of Nevada sand ($D_r = 60\%$)

614 Figure 14: Drained CADC tests with constant p' on Nevada sand

615 Figure 15: Drained CADC tests with constant q on Nevada sand

616 Figure 16: Drained tests on Toyoura sand

617 Figure 17: Undrained tests on Toyoura sand

618 Figure 18: Stress paths used for tests on Toyoura sand (Pradhan *et al.*, 1989a)

619 Figure 19: Drained tests with various stress paths on Toyoura sand

620 Figure 20: Drained cyclic test on a loose sample of Toyoura sand

621 Figure 21: Drained cyclic test on a dense sample of Toyoura sand

622 Figure 22: Drained cyclic test on a very loose sample of Toyoura sand

623 Figure 23: Drained cyclic test on a very loose sample of Toyoura sand

624 Figure 24: Undrained cyclic test with constant cyclic amplitude

625 Figure 25: Undrained cyclic test with irregular cyclic amplitude

626

627 **Table 1: Material constants used in all simulations**

Soil	Reference	κ	ν	M_{cs}	λ_0	λ_{cr}	p'_{cr} (kPa)	Γ_0	N	R	k	A
Nevada Sand	Arulmoli *et al.* (1992)	0.003	0.33	1.25	0.022	0.24	2000	1.910	1.5	3.0	2.0	1.5
Toyoura Sand	Verdugo and Ishihara (1996) & Pradhan *et al*. (1989a&b)	0.008	0.3	1.24	0.033	0.24	2000	2.075	2.5	8.5	2.0	1.0
Fuji River Sand	Ishihara *et al.* (1975)	0.01	0.3	1.48	0.032	0.21	1500	1.870	3.0	6.2	2.0	1.0

628

629

630 **Table 2: Values of k_m parameter used in different simulations**

Soil	k_{m0}		β_1	β_2
	First time loading	Unloading & reloading		
Nevada Sand	6.2	115.8	0.95	0.34
Toyoura Sand	1.2	76.0	1.05	0.3
Fuji River Sand	2.0	18.0	0	0

631

632

633 **Table 3: State parameters used in simulation of cyclic tests**

Soil Type	Test Type	Sample/Load Condition	ID	υ_0	p'_0 (kPa)
Toyoura Sand	Drained $p' = cst$	Loose	1	1.845	98.1
		Dense	2	1.653	
		Very Loose	3	1.865	
		Very Loose	4	1.855	
Fuji River Sand	Undrained cyclic	Constant Amplitude	1	1.735	212.6
		Irregular Amplitude	2	1.749	156.0

634

635

636